DTU Library

Wind energy applications of synthetic aperture radar

Badger, Merete

Publication date:
2006

Document Version
Publisher's PDF, also known as Version of record

[Link back to DTU Orbit](#)

Citation (APA):
Badger, M. (2006). Wind energy applications of synthetic aperture radar. Risø National Laboratory. Risø-PhD, No. 27(EN)

Wind Energy Applications of Synthetic Aperture Radar

Merete Bruun Christiansen

Author: Merete Bruun Christiansen
Title: Wind Energy Applications of Synthetic Aperture Radar
Department: Wind Energy Department

This thesis is submitted in partial fulfillment of the requirements for the Ph.D. degree at University of Copenhagen.

Abstract (max. 2000 char.):

Synthetic aperture radars (SAR), mounted on satellites or aircraft, have proven useful for ocean wind mapping. Wind speeds at the height 10 m may be retrieved from measurements of radar backscatter using empirical model functions. The resulting wind fields are valuable in offshore wind energy planning as a supplement to on site measurements, which are costly and sparse, and model wind fields, which are not fully validated. Two applications of SAR measurements in offshore wind energy planning are addressed here: the study of wind farm wake effects and the potential of using SAR winds in offshore wind resource assessment. Firstly, wind wakes behind two large offshore wind farms in Denmark – Horns Rev and Nysted – are identified. A region of reduced wind speed is found downstream of both wind farms from the SAR wind fields. The wake extent and magnitude depends on the wind speed, the atmospheric stability, and the fraction of turbines operating. Wind farm wake effects are detected up to 20 km downwind of the last turbine. This distance is longer than predicted by state-of-the art wake models. Wake losses are typically 10-20% near the wind farms. Secondly, the potential of using SAR wind maps in offshore wind resource assessment is investigated. The resource assessment is made through Weibull fitting to frequency observations of wind speed and requires at least 100 satellite observations per year for a given site of interest. Predictions of the energy density are very sensitive to the wind speed and the highest possible accuracy on SAR wind retrievals is therefore sought. A 1.1 m s^{-1} deviation on the mean wind speed is found through comparison with mast measurements at Horns Rev. The accuracy on mean wind speeds and energy densities found from satellite measurements varies with different empirical model functions. Additional uncertainties are introduced by the infrequent satellite sampling at fixed times of the day. The accuracy on satellite based wind resource assessment is sufficient in the early stage of wind farm planning, before higher-accuracy on site measurements are available.

Table of contents

Papers:

I   Christiansen, M.B., & Hasager, C.B. (2005). Wake effects of large offshore wind
        farms identified from satellite SAR. *Remote Sensing of Environment, 98*, 251-
        268.

II   Christiansen, M.B., & Hasager, C.B. (2006). Using airborne and satellite SAR for
        wake mapping offshore. *Wind Energy, 9*, 437-455.

III   Christiansen, M.B., Koch, W., Horstmann, J., Hasager, C.B., & Nielsen, M.
        (2006). Wind resource assessment from C-band SAR. *Remote Sensing of
        Environment, 105*, 68-71.

IV   Hasager, C.B., Barthelmie, R.J., Christiansen, M.B., Nielsen, M., & Pryor, S.C.
        (2006). Quantifying offshore wind resources from satellite wind maps: study area
        the North Sea. *Wind Energy, 9*, 63-74.

V   Monaldo, F.M., Thompson, D.R., Winstead, N.S., Pichel, W.G., Clemente-
        Colón, P, & Christiansen, M.B. (2006). Ocean wind field mapping from synthetic
        aperture radar and its application to research and applied problems. *Johns
        Hopkins APL Technical Digest, 26*, 102-113.

VI   Christiansen, M.B. (2004). Wind energy studies offshore using satellite remote
        sensing. 19th World Energy Congress 2004, Sydney (AU), 5-9 Sep 2004.
        Unpublished. 10 p.

VII   Christiansen, M.B. & Hasager, C.B. (2005). Wake studies around a large offshore
        wind farm using satellite and airborne SAR. In: Proceedings (CD-ROM). 31st
        International Symposium on Remote Sensing of Environment: Global Monitoring
        for Sustainability and Security, St. Petersburg (RU), 20-24 Jun 2005. (Nansen
        International Environmental and Remote Sensing Centre, St. Petersburg, 2005) 4
        p.

VIII   Christiansen, M.B. & Hasager, C.B. (2006). Wind energy applications of
        synthetic aperture radar. In: Combined preprints (CD-ROM). 86th AMS Annual
        Meeting, Atlanta, GA (US), 29 Jan - 2 Feb 2006. (American Meteorological
        Society, Boston, MA, 2006) 6 p.

Preface

This Ph.D. dissertation was submitted in March 2006 to the Faculty of Science, University of Copenhagen. The Ph.D. defense took place in August 2006. The dissertation is the result of a three-year project carried out in collaboration between the Institute of Geography, University of Copenhagen (IGUC), the Wind Energy Department at Risø National Laboratory, and Ørsted-DTU at the Technical University of Denmark. Within the project, 4.5 months were spent at the Johns Hopkins University, Applied Physics Laboratory (JHU/APL) in Maryland, USA, and two weeks were spent at GKSS Research Center in Geestacht, Germany. The dissertation consists of a synopsis followed by a collection of five journal papers and three conference proceedings papers. In addition to the written material, achievements within the project have been presented at scientific meetings and workshops.

The Ph.D. project was funded by Risø National Laboratory and the Danish Technical Research Council through the projects SAT-WIND (STVF 2058-03-0006) and SAR-WAKE (STVF 26-02-0312). Satellite scenes were obtained from the European Space Agency within Cat. 1 project EO-1356. Elsam A/S is thanked for the meteorological measurements, used throughout the project, and for wind farm production data from Horns Rev. Other contributors of data are acknowledged in the relevant papers.

I wish to thank my advisors Inge Sandholt at IGUC and Henning Skriver at Ørsted-DTU for help and suggestions throughout the project. Special thanks go to Charlotte Bay Hasager, my supervisor at Risø, who has been involved in every step of the project work, providing invaluable support. Thanks for the dedication and for being a great inspiration. Jake Badger, also from Risø, deserves warm thanks for helping out with programming issues, mapping, and proof reading. The rest of the Meteorology group at the Risø Wind Energy Department is thanked for providing an ideal working environment.

At JHU/APL, the Ocean Remote Sensing group is kindly thanked for the hospitality and for giving me a very interesting stay abroad. In particular, I am grateful to Frank Monaldo and Donald Thompson for all the helpful advice and discussions on SAR-related issues. At GKSS Research Center, Jochen Horstmann and Wolfgang Koch are thanked for hosting me and for the fruitful collaboration on SAR wind retrievals.

1 Introduction

The wind as an energy resource has been increasingly in focus over the past decades, starting with the global oil crisis in the 1970s. The rapidly growing demand for energy in the world, combined with ambitious targets set for the reduction of greenhouse gas emissions, call for a further exploitation of renewable energy resources. The total installed wind power capacity worldwide was 48 GW by the end of 2004 with an annual growth rate of 28% (IEA, 2005). Tnhe electricity generated in 2004 amounted to the annual consumption of Portugal and Greece combined. Europe accounts for the majority of the world's installed wind power; Germany and Spain have the largest absolute capacity and Denmark the largest capacity per person. In Denmark, wind power amounts to ~20% of the total electricity generation.

The possibility of expanding wind power production to offshore locations is attractive, especially in northern Europe where the density of wind turbines on land is high. Further expansion on land relies on replacement of existing turbines with larger-capacity models. There is an upper limit to the turbine size acceptable by the general public on land, both in terms of tower height and capacity. In contrast, very large turbines can be deployed offshore with a minimal noise impact and visual disturbance. The increased cost of offshore constructions is counteracted by a higher energy production. For example, the number of full-load hours per year can double offshore compared to the average for wind turbines on land. The fatigue load on turbines is lower offshore due to reduced turbulence intensity (Frandsen & Thomsen, 1997). However, the properties of the marine atmospheric boundary layer are not as well understood as the boundary layer over land, owing to a limited amount of meteorological observations. Offshore mast are few and costly, whereas observations from ships and ocean buoys suffer from flow distortion and represent very low levels within the atmospheric boundary layer (Brown, 2000b).

High-resolution ocean wind fields can be retrieved from synthetic aperture radars (SAR) mounted on satellites or aircraft. Conceptually, these imaging radars are capable of sensing small scale ripples at the sea surface, generated by the local wind. Through empirical relationships, the radar measurements can be converted to wind speed at 10 m. The concept of SAR wind retrieval was well determined and validated, when this Ph.D. project was initiated in 2003. For example, Risø National Laboratory (hereinafter Risø) participated in the project WEMSAR (2000-2003), which involved validation of a series of SAR wind maps against model data and in situ measurements from an offshore meteorological mast (Hasager et al., 2002; 2004). The use of SAR wind fields for practical applications was limited at the time. The goal of this Ph.D. project was therefore to investigate potentials and limitations related to the application of SAR measurements in offshore wind energy.

Two major applications of SAR wind fields were identified. One was the quantification of wake effects (i.e. regions of reduced wind speed and enhanced turbulence intensity) downstream of large offshore wind farms. Knowledge about the wind farm wake effect becomes increasingly more important with the prospect of locating future offshore wind farms in clusters. The problem has previously been addressed through wake modeling (Barthelmie et al., 2004a; Frandsen et al., 2006) and, to a limited extent, in situ measurements (Barthelmie et al., 2003b; 2006). Hypothetically, the spatial variation in wind speed obtained from SAR measurements should be very useful for defining the magnitude and spatial extent of wind wakes. This hypothesis led to a study of wind wakes

downstream of two large offshore wind farms in Denmark from a series of SAR scenes acquired by satellites and aircraft.

The second application investigated was wind resource assessment from satellite SAR. Satellite wind maps provide unique spatial information over large areas (up to 500 km x 500 km per image) and the availability of images is generally increasing over time at a decreasing cost. Implementation of SAR images in the early stages of wind farm planning is thus becoming realistic. Parallel to this Ph.D. project, Risø was responsible for developing a software tool within the project EO-WINDFARM (2003-2006). The tool handles all aspects of wind resource assessment, once SAR wind fields are available as input. The resource assessment is very sensitive to wind speed, therefore SAR winds should be retrieved as accurately as possible for wind resource applications. The specific problem addressed in the Ph.D. project was how to achieve the optimum data input for wind resource assessment.

This thesis consists of a synopsis followed by a collection of papers. The Ph.D. project embraces elements of wind energy, radar technology, and meteorology. Hence, the objective of the synopsis is to introduce a broad readership to the theoretical background, methods and results of the Ph.D. work within each of these topics. Further, the synopsis provides state-of-the-art information on offshore wind energy and ocean remote sensing; both areas are currently going through a rapid technological development. The synopsis is organized as follows: Section 2 gives an introduction to offshore wind farming with special emphasis on the sites studied within this project. Section 3, describes the principle of SAR and Section 4 provides details on the platforms and sensors used in this project. Important characteristics of SAR imagery are outlined in Section 5, and the concept of SAR wind retrieval is described in Section 6. Atmospheric and oceanic parameters having a potential influence on SAR measurements are described in Section 7 and 8, respectively, using examples from the project. Finally, the application of SAR wind fields in offshore wind energy is addressed in Section 9 concerning wind farm wake effects and Section 10 about wind resource assessment. A brief introduction to each paper is given in Section 11 followed by conclusions and future perspectives in Section 12.

Five journal papers systematically deal with the main issues of the Ph.D. project. Paper I is on the quantification of wind farm wake effects from satellite SAR images and has been published in *Remote Sensing of Environment*. Paper II describes an airborne SAR campaign, which was conducted to obtain more detail on the wind farm wake effect. The paper has been accepted for publication in *Wind Energy*. Paper III is on wind resource assessment from SAR and, more specifically, on optimizing the data input. This paper has been submitted to *Remote Sensing of Environment*. Paper IV reviews recent work carried out at Risø in the field of wind energy and satellite remote sensing, including SAR and other sensors. A comparison study is made between SAR measurements and a wind farm wake model. The paper has been published in *Wind Energy*. Paper V gives an overview of SAR wind retrieval and two applications are described: the measurement of barrier jets and wind power production. It has been accepted for publication in *Johns Hopkins APL Technical Digest*. Three additional papers (VI-VIII) are included in the thesis. These papers have been presented at international conferences. Paper VI describes current challenges of the energy industry and places the Ph.D. study in a broader context with figures on the global wind power status. The papers VII and VIII are overviews of the Ph.D. project, providing additional figures on wind farm wake effects and wind resource assessment from SAR.

2 Offshore wind farming

The world's first offshore wind farm was built as a pilot project in 1991 at Vindeby in Denmark. The Vindeby farm consists of 11 turbines each with a capacity of 450 kW. Hub-heights are 38 m and rotor diameters 35 m. The wind farm is located with a minimum distance of 2 km offshore. A lot of knowledge on offshore wind farming has been gained from extensive measurement campaigns at the Vindeby site (Barthelmie et al., 2004a; 1994; 1996; 2003b; Frandsen et al., 1996). A second pilot project was carried out at Tunø Knob from 1995 onwards. These turbines were slightly larger (500 kW) compared to Vindeby and a similar total capacity could thus be achieved with 10 turbines.
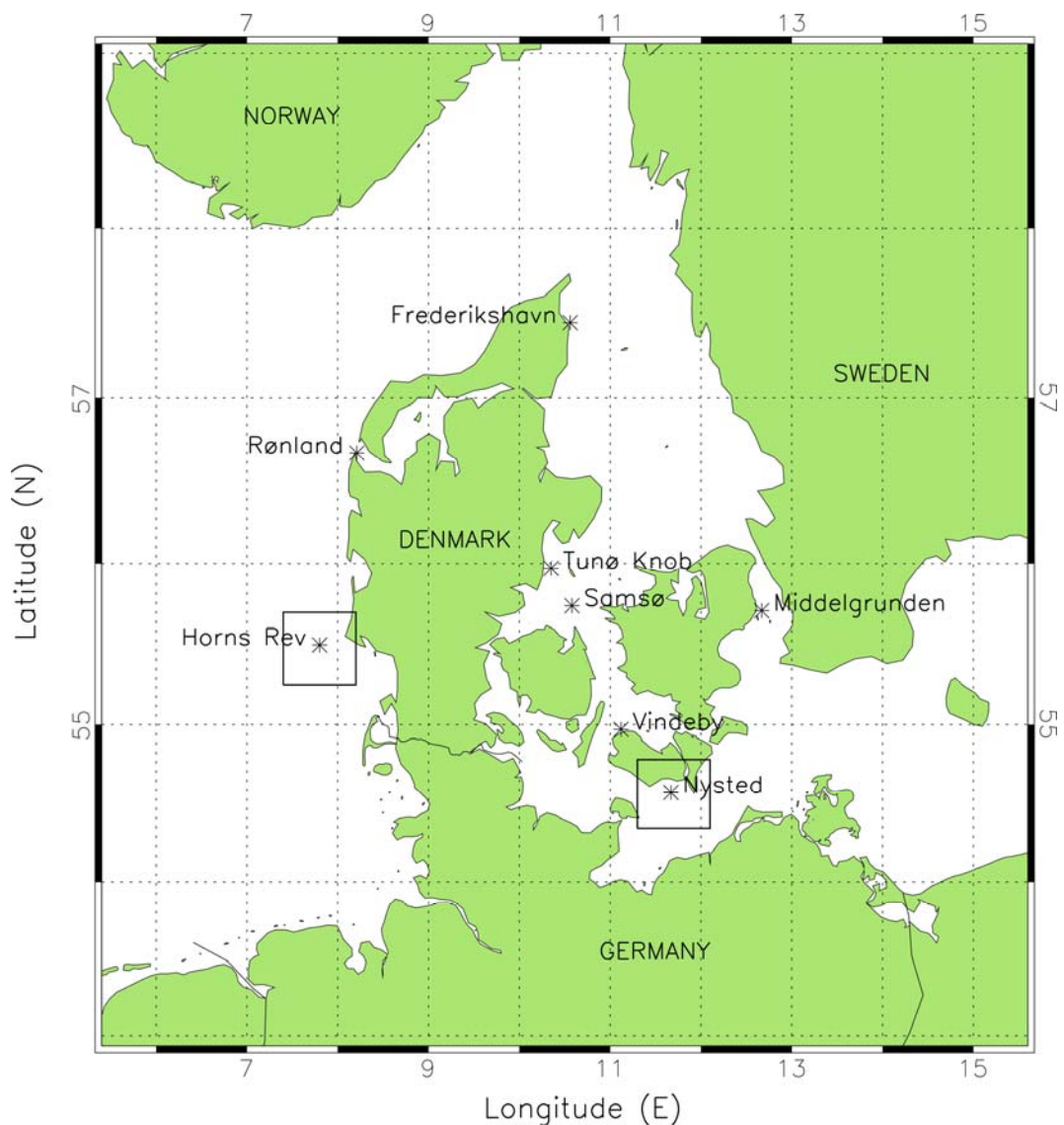

Figure 2-1. Map showing the location of offshore wind farms in Denmark. The wind farms at Horns Rev and Nysted were investigated in this project. At both sites, a second wind farm is planned to be operational before 2010. Square boxes indicate the areas covered by Figure 2-2.

A major expansion of Danish offshore wind energy has taken place in the present century, starting with the construction of Middelgrunden offshore wind farm in Copenhagen in 2001. A total of eight offshore wind farms are currently operating in Denmark; Figure 2-1 shows the wind farm locations. Offshore wind farms are also operating in the UK, Ireland, and Sweden. Germany and the Netherlands have near-shore wind farms within ~500 m from the coastline. Other counties with advancing offshore plans include China and the US. Turbine capacities have increased up to 3 MW and the trend is towards even larger capacities. For example, 5 MW turbines have been deployed at Høvsøre, a test site on the Danish west coast run by Risø. Research is ongoing to estimate the consequence of installing turbines up to 12 MW (http://www.risoe.dk/vea-atu/remote/12mw.htm). Turbine hub heights have generally increased with the growing capacity and are around 70 m for the most recent offshore wind farm installations. This height is expected to increase with up to 100 m for the 12 MW installations described above.

Describing the atmospheric boundary layer conditions aloft is one of the major challenges related to the deployment of very large turbines. Measurements at the Høvsøre test station have shown that the wind speed profile deviates from the logarithmic profile (see Section 7.1) for heights above 50 m (Gryning et al., 2006). Another challenge is moving to deeper waters to utilize the increasing wind resource with distance offshore. Current wind farms are installed at water depths up to ~20 m but new foundation types, including floating platforms, are under development (IEA, 2005). Finally, challenges are related to the integration of large scale wind power in the electrical grid (Koch et al., 2003a; 2003b) and to accurate short-term prediction of wind power production offshore (Barthelmie & Giebel, 2006; Giebel et al., 2003).

2.1 Horns Rev and Nysted offshore wind farms

Horns Rev and Nysted offshore wind farms, operated by Elsam A/S and Energy E2 A/S respectively, were chosen as study sites for this project. The two wind farms are the largest in the world and were built as demonstration projects. A monitoring program has run since 1999 to identify environmental impacts of large scale offshore wind farming. Results of the monitoring are available at http://www.hornsrev.dk (Horns Rev) and http://uk.nystedhavmoellepark.dk (Nysted). At Horns Rev, 80 Vestas turbines (2 MW) started operating in December 2002. The wind farm is located 14-20 km offshore at water depths of 5-15 m. At Nysted, 72 Bonus turbines (2.3 MW) became operational in December 2003. These turbines are located 10-13 km offshore at water depths of 6-10 m. The electricity supply, provided by each of the wind farms at Horns Rev and Nysted, amounts to the consumption of ~145000 households. Figure 2-2 shows the turbine layout for the two wind farms, as seen from the ERS-2 satellite. Further details on the two wind farm sites are given in Paper I.

Future developments at Horns Rev and Nysted
In 2004, a call for tenders was made for two additional wind farms; one at Horns Rev and one at Nysted. Energy E2 A/S won the right to install and operate a 200 MW wind farm at Horns Rev with an expected start of operation in 2009. The Nysted tender, also for a 200 MW wind farm, is to be concluded in 2006 (Danish Energy Authority, 2005). A screening has identified a further four potential sites for large scale offshore wind farming in Denmark.
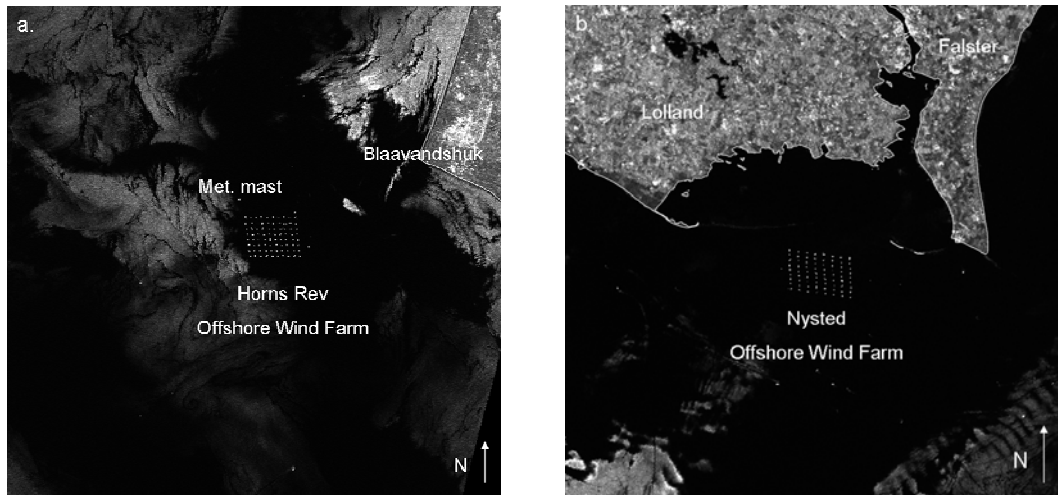
Figure 2-2. Images from the ERS-2 satellite showing a) the wind farm at Horns Rev in the North Sea (16 March 2003), and b) the wind farm at Nysted in the Baltic (17 August 2004). Each image covers 50 km x 50 km; see Figure 2-1 for location.

Figure 2-3. Photograph of the 62 m tall meteorological mast M2 at Horns Rev, erected in 1999. The mast position 2 km to the north of the wind farm is indicated in Figure 2-2. Photo courtesy Paul B. Sørensen, Elsam Engineering A/S.

Meteorological measurements at Horns Rev

An offshore meteorological mast was erected at Horns Rev in 1999 by Elsam A/S. The mast is located 2 km to the north of the wind farm (see Figure 2-2 (a)). Data from the mast were available for this project and the following measurements were used: wind speed (15, 30, 45, and 62 m), wind direction (28, 43, and 60 m), turbulence intensity (62 m), air temperature (13 and 55 m), and the water temperature at -4 m. All measurements are stored as 10 minute mean values. Wind speed measurements at the three lower levels are obtained simultaneously from two anemometers positioned on a horizontal boom. The booms have an orientation of 45/225° and are seen in the photograph, Figure 2-3. By consequently selecting the upwind anemometer, flow distortion was minimized.

3 Synthetic aperture radar

Synthetic aperture radar (SAR) is an active remote sensing technique. SAR sensors are mounted on moving platforms, such as satellites or aircraft. They illuminate an area on the Earth surface by transmitting pulses of energy in the microwave spectrum. Images are formed from precise measurements of the time delay and Doppler shift of the returned radar signal (Ulaby et al., 1982). The most common SAR bands are listed in Table 3-1.

Band	Wave length [cm]	Frequency [GHz]
L	15-30	1-2
S	8-15	2-4
C	4-8	4-8
X	2.5-4	8-12

Table 3-1. Wave length and frequency for selected radar bands.

SAR pulses penetrate clouds and light rain and data acquisition is possible day or night, independently of sunlight. SAR signals are electromagnetic waves with a polarization determined by the orientation of the electric field. The polarization may be vertical (V) or horizontal (H) and is always perpendicular to the direction of wave propagation. In the following, a C-band SAR, which is vertically polarized in both transmit and receive, is denoted C_{VV}. Accordingly, the same SAR with horizontal polarization is denoted C_{HH}.

3.1 Imaging geometry

Figure 3-1 illustrates the geometry of SAR imaging. The radar beam is typically orthogonal to the azimuth (i.e. flight) direction. The direct distance from the radar to a ground target is termed slant-range, whereas the corresponding distance on the ground is the ground range. The entire span of ground range distances, covered by a radar, is the swath width. The radar incidence angle, θ is defined relative to the vertical plane and θ is thus smaller in the near range compared to the far range.

Spatial resolution determines the minimum distance between objects, necessary to distinguish the objects within radar images. In slant range, the spatial resolution, $\Delta R_{slant-range}$ depends on bandwidth only:

$$\Delta R_{slant-range} = \frac{c}{2B} \tag{3.1}$$

where c is the speed of light and B is the bandwidth of the radar signal.
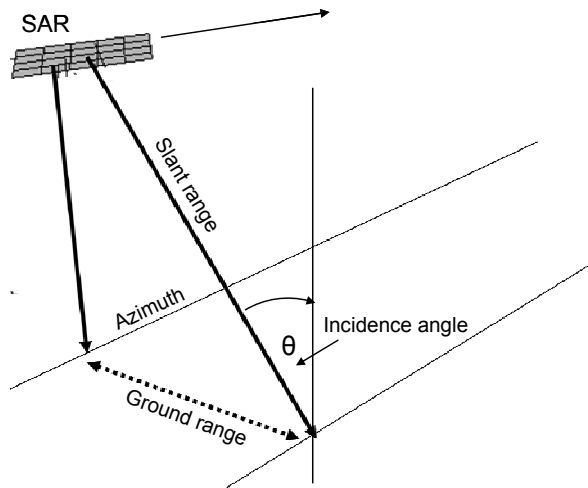
Figure 3-1. SAR imaging geometry.

The slant range resolution is easily converted to ground range resolution, $\Delta R_{ground\text{-}range}$ through the relationship:

$$\Delta R_{ground-range} = \frac{\Delta R_{slant-range}}{\sin \theta} \qquad (3.2)$$

where θ is the radar incidence angle. Further re-sampling is necessary to obtain a uniform pixel size over the swath.

In the azimuth direction, the spatial resolution achievable with a SAR is much higher than for the simpler real aperture radar (RAR). Conceptually, the azimuth resolution depends on the radar beam width. As the beam fans out with increasing distance from a radar, the spatial resolution decreases. In addition to the range, the beam width depends on the radar wavelength and the antenna length in the azimuth direction. A high spatial resolution can be achieved by increasing the antenna length, physically or synthetically. The key principle of SAR is to utilize the forward motion of the platform to synthesize a long antenna. As the SAR moves forward, a series of pulses is transmitted and received such that any given surface target is illuminated many times. Images are reconstructed through advanced signal processing, which includes weighting of the many contributions per target to form a long synthetic aperture. The spatial resolution in the azimuth direction, $\Delta R_{azimuth}$ for the SAR is then:

$$\Delta R_{azimuth} = \frac{L}{2} \qquad (3.3)$$

where L is the antenna length. $\Delta R_{azimuth}$ is now independent of range.

3.2 Scattering mechanisms

The amount of backscattering from the Earth surface to a radar depends, among other things, on the radar incidence angle and the surface roughness (e.g. Ulaby et al. (1982)). There is a general fall-off of the measured radar backscatter at increasing incidence angles. For smooth surfaces, specular reflection is dominant. The radar backscatter is very limited, as the reflection is directed away from the surface at an angle corresponding to the angle of incidence (Figure 3-2a). Sea surfaces typically act as direct scatterers under calm wind conditions. An exception is when objects (e.g. wind turbines) cause double bouncing of the radar pulse such that a very strong signal is returned to the radar (Figure 3-2b). Such objects are known as dihedral corner reflectors and are useful in radar calibration (Raney, 1998).
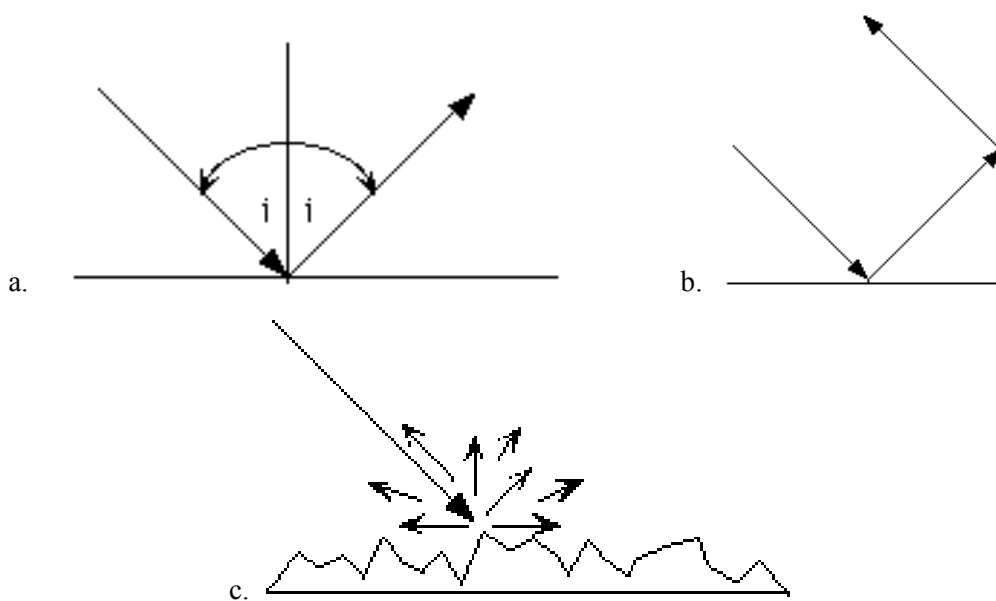
Figure 3-2. Scattering from a) a smooth surface, b) a corner reflector, and c) a rough surface (modified from http://envisat.esa.int/dataproducts/asar/CNTR.htm, ASAR Product Handbook).

For rough surfaces, Bragg scattering is dominant (Valenzuela, 1978). Bragg resonance occurs through interaction of the radar signal with surface elements comparable in size to the radar wave length. For oceans, the radar signal interacts with cm-scale capillary and short-gravity waves. This is expressed in the relation:

$$\lambda_{Bragg} = \frac{\lambda_{radar}}{2 \sin \theta} \tag{3.4}$$

where λ_{Bragg} and λ_{radar} are the Bragg and radar wave lengths, respectively, and θ is the radar incidence angle. Strong backscattering occurs when Equation 3.4 is fulfilled for a given radar wavelength and incidence angle. Bragg scattering is diffuse, as illustrated in Figure 3-2c. The portion of scattering directed back to the radar instrument per area is the backscatter coefficient (σ^0), or the normalized radar cross section (NRCS).

4 Platforms and sensors

4.1 Satellite SAR

The first space-borne SAR was the American SEASAT, operated in June-October 1978. SEASAT was an L_{HH} SAR designed mainly for ocean and ice applications. It was followed up by the derivative Shuttle Imaging Radars SIR-A and SIR-B in 1981 and 1984, respectively. The second satellite SAR was launched with ERS-1 in 1991 by the European Space Agency (ESA). This SAR operated in C_{VV} as the identical ERS-2 SAR launched in 1995. Other satellite SARs launched in the 1990s include the Russian ALMAZ with an S_{HH} SAR, the Japanese JERS-1 with an L_{HH} SAR, and the Canadian RADARSAT-1 with a C_{HH} SAR. ALMAZ and RADARSAT-1 were the first satellite SAR sensors capable of scanning at various radar incidence angles. Envisat was launched by ESA in 2002, as follow-on to the ERS-1/2 missions. Envisat has an advanced SAR (ASAR), which scans in one of the four polarization combinations C_{VV}, C_{HH}, C_{HV}, or C_{VH}. The L-band PALSAR, launched on the Japanese ALOS satellite in early 2006, is the first fully polarimetric spaceborne SAR, which means it can operate at the four polarization combinations simultaneously. RADARSAT-2, which is scheduled for launch in 2006, will have the same capability in C-band.

Satellite	Country	Period	Band	Polarization
SEASAT	USA	Jun. - Oct. 1978	L	HH
ERS-1	Europe	Jul. 1991 - Mar. 2000	C	VV
ALMAZ	USSR	March 1991 - Oct. 1992	S	HH
JERS-1	Japan	Feb. 1992 - Nov. 1998	L	HH
ERS-2	**Europe**	**Mar. 1995 - present**	**C**	**VV**
RADARSAT-1	Canada	Nov. 1995 - present	C	HH
ENVISAT	**Europe**	**Mar. 2002 - present**	**C**	**HH, HV, VH, VV**
ALOS	Japan	Jan. 2006 - present	L	Full
RADARSAT-2	Canada	Launch scheduled for 2006	C	Full

Table 4-1. Summary of satellite SAR systems. The two systems used in this project are highlighted.

Table 4-1 summarizes the history of satellite SAR systems. All of the platforms listed are polar-orbiting, sun-synchronous satellites meaning that they pass over a given location on the Earth at a fixed time for each ascending (northbound) and descending (southbound) orbit. The principle is illustrated in Figure 4-1. The satellite altitude is typically ~800 km. In addition to the satellite missions described here, a number of space shuttle missions have been carried out at altitudes of ~200 km, starting with SIR-A and SIR-B. The satellite scenes used in this project were acquired from ERS-2 and Envisat. In the following, a description of the two platforms and their SAR sensors is given.
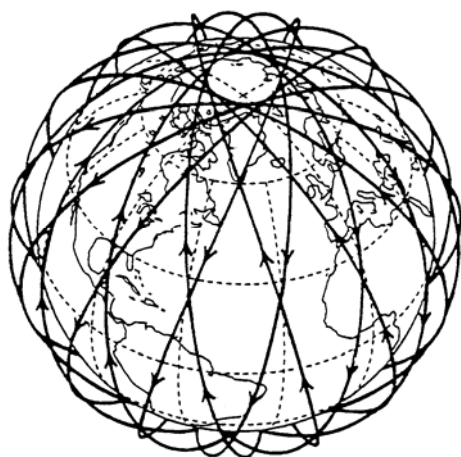
Figure 4-1. Diagram showing the trajectory of polar orbiting satellites. Arrows indicate ascending (northbound) and descending (southbound) overpasses.

ERS-2 SAR

Despite a scheduled lifetime of 3 years, ERS-2 has now orbited the Earth for more than 10 years. The ERS-2 repeat cycle (i.e. the time between fully identical orbits) is 35 days. A given location in Denmark is covered approximately every 10 days. Ascending scenes are acquired around 10:30 UTC and descending scenes around 21:30 UTC. The SAR on board ERS-2 operates in strip-map mode meaning that a 100 km swath is covered at incidence angles of 20-26° at any given time. The 3-look precision images used in this project have a spatial resolution of ~25 m (the concept of looks is addressed further in Section 5.1). Calibration of ERS-2 SAR data to the normalized radar cross section (NRCS) involves several correction steps (e.g. ADC compensation, antenna pattern correction). These steps are included in the Basic Envisat SAR Toolbox (BEST) provided by ESA (http://envisat.esa.int/services/tools_table.html). The toolbox was used to retrieve NRCS from ERS-2 scenes for the work presented in Paper I and II. ERS-2 SAR scenes acquired in 1999-2005 were purchased for this project. The majority were acquired over Horns Rev in the North Sea but some of the most recent scenes were acquired over Nysted in the Baltic.

Envisat ASAR

Envisat has orbit dynamics similar to ERS-2. In strip-map mode the ASAR instrument scans in one of seven available swaths (IS1-IS7). The swaths are 56-105 km wide and have a total incidence angle span of 15-45°. Data may be acquired in 4-look image mode (IMG) in C_{VV} or C_{HH}, as illustrated in Figure 4-2 (left). Alternatively, data may be obtained in C_{VV} and C_{HH} simultaneously, using the 2-look alternating polarization mode (APP) shown in Figure 4-2 (center). Strip-map data have a spatial resolution of ~30 m. Envisat may also be operated as a ScanSAR capable of scanning in a 400 km 7-look wide swath mode (WSM), see Figure 4-2 (right). The spatial resolution is then ~150 m. Data acquired in the three modes IMG, APP, and WSM were used in this project. The ASAR instrument also has a global monitoring mode and a wave mode. Preliminary results have shown that the latter may suitable for global coverage ocean wind mapping in the future (Horstmann et al., 2003).
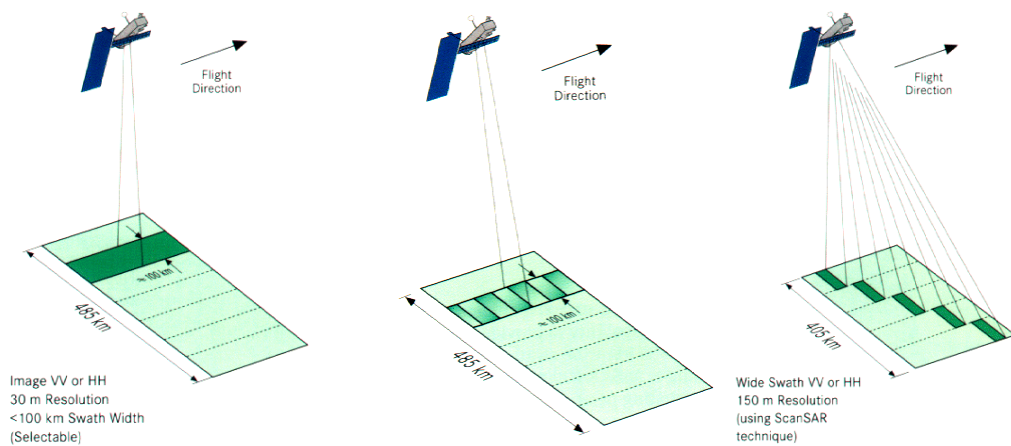
Figure 4-2. Diagram showing selected Envisat ASAR modes of operation. Left: image mode (IMG), center: alternating polarization mode (APP), and right: wide swath mode (WSM).

4.2 Aircraft SAR

Numerous airborne SAR campaigns have been conducted parallel to the development of satellite SARs. A major advantage of airborne SAR compared to satellite SAR is the higher degree of flexibility in the planning of experiments. For example, data acquisition may be scheduled according to the wind conditions. Further, many airborne SAR platforms are capable of operating with several combinations of frequency and polarization. The swath width of airborne systems is much smaller than satellite SAR swaths. However, the low altitude of airborne platforms compared to satellites allows a broader span of incidence angles and a much higher spatial resolution. Airborne SAR data are very suitable for fundamental research purposes and sensor development, whereas satellites are needed for the monitoring of larger areas.

A review of airborne SAR systems is given by e.g. Raney (1998). Examples of airborne SAR systems include the American AirSAR, Canadian C/X SAR and STAR-1. In Europe, the Technical University of Denmark (DTU) has developed EMISAR and the German Aerospace Centre (DLR) has developed an Experimental SAR (E-SAR). The latter was used in this project, as described in the following.

E-SAR
A campaign was conducted over the wind farm at Horns Rev on 12 October 2003 with data acquisitions in C_{VV}, C_{HH}, and fully polarimetric L-band. Note that E-SAR is also capable of operating in X, S, and P band. For wind retrievals in this project, the C-band data were used. During the experiment, the E-SAR was mounted on the Dornier aircraft pictured in Figure 4-3. Data were acquired in two wind-aligned and three crosswind tracks, as outlined in Figure 4-4 (see Paper II for details). Incidence angles were 26-55° and the spatial resolution was 2 m.

Figure 4-3. Photograph of the Dornier DO-228 aircraft used for the E-SAR campaign over Horns Rev on 12 October 2003. Positions of the C-band and L-band SAR sensors are indicated (from http://www.dlr.de/hr/institut/abteilungen/sar-technologie/fg/flugzeug-sar/)
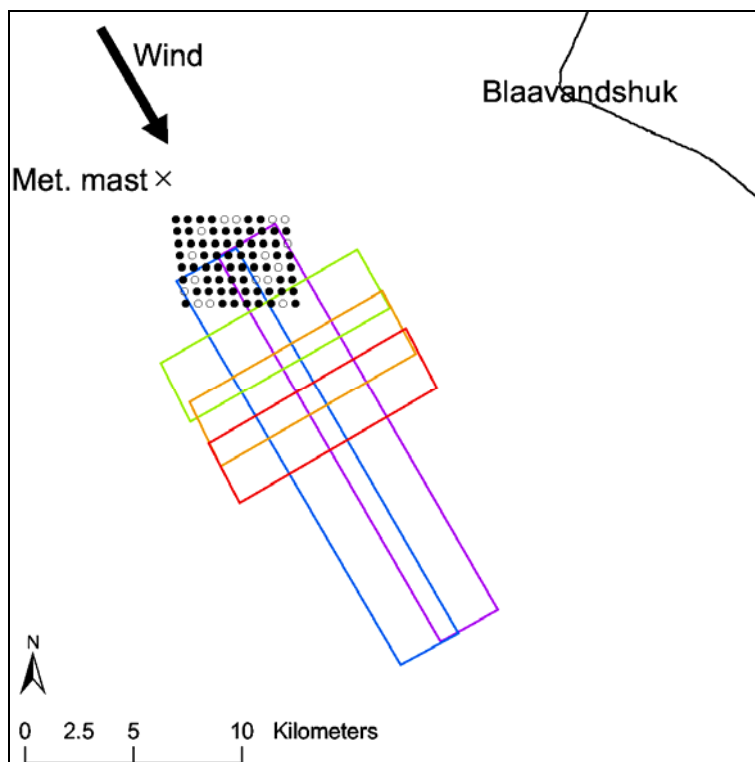

Figure 4-4. Layout of five overlapping aircraft tracks (coloured), wind turbines (circles, filled if running), and the meteorological mast (x) at Horns Rev. The wind direction was ~330° and the wind speed 8-10 m s^{-1} (from mast) during the E-SAR campaign on 12 October 2003.

4.3 Other Earth observation data

This project is based mainly on high-resolution SAR data. Other types of microwave Earth observation data (i.e. scatterometry and passive microwave) have been investigated at Risø in the project SAT-WIND (2004-2005). A brief description of these data, and their potential use in wind energy, is given in the following. The section on platforms and sensors ends with a description of optical sea surface temperature data from the Moderate Resolution Imaging Spectroradiometer (MODIS) that was used in the Ph.D. project.

Scatterometry
In Paper IV, results from scatterometer data are described. The measurements are from the Quickscat instrument operated by the National Aeronautics and Space Administration (NASA). Quickscat has provided a daily global coverage since 1997. Wind products are based on the same principles as high-resolution SAR measurements, except the wind speed and direction are obtained simultaneously using multiple antennas. Other advantages of scatterometer data to high-resolution SAR include the frequent overpasses (twice per day) and that data are available at no cost. This means a large number of samples may be collected for a given area of interest, which is useful in wind resource assessment studies (see Section 10). Disadvantages include a much coarser resolution compared to SAR data (0.25° x 0.25° for Quickscat), and the masking of near-shore areas in a ~50 km wide zone. The latter is a major limitation in wind energy studies, as offshore wind farms are typically built within this zone. Scatterometers are thus most valuable for investigations of the wind climate on a regional scale (e.g. for the Danish seas). Very useful estimates of the inter-annual wind climate variability can be obtained from scatterometer data (Paper IV and Hasager et al. (2006)).

Passive microwave
Passive microwave sensors measure brightness temperatures and rely on natural radiation from the Earth surface. The brightness temperatures are related to the surface wind speed. Wind speed products from the Special Sensor Microwave Imager (SSM/I) provide very long time series with several overpasses per day. Wind directions are not available from the instrument. Hasager et al. (2006) have analyzed SSM/I data for Denmark covering a ten-year period (1995-2005). The data have a spatial resolution similar to Quickscat but with a wider coastal mask. The use of SSM/I is thus restricted to open oceans with the same applications as described for scatterometry.

Sea surface temperature measurements from MODIS Aqua
Two MODIS instruments are currently in orbit on the platforms Terra and Aqua, providing a morning and evening scene, respectively. A number of standard MODIS products are available for download through NASA's Earth Observation Systems Gateway (http://edcimswww.cr.usgs.gov/pub/imswelcome). A sea surface temperature (SST) product was obtained from MODIS Aqua over Denmark for 12 October 2003 at 11:50 UTC. This was shortly after the campaign with airborne E-SAR over Horns Rev ended. The purpose was to use the SST data to determine the air-sea temperature difference and thus the atmospheric stability at the time of the E-SAR campaign (see Section 7.3). The MODIS scene was acquired at 4 μm (infra-red) with a coverage of 1200 km x 1200 km and a spatial resolution of 1 km. Latitude and longitude was provided with the product for each image pixel along with a flag for quality checking.

5 SAR image characteristics

Figure 5-1 shows a NRCS image from the E-SAR campaign at Horns Rev. Bright image pixels indicate a high level of backscattering. Several image characteristics, typical for SAR measurements, are noticed and will be described in the following.

Figure 5-1. NRCS image acquired in C_{VV} along a wind-aligned E-SAR track (see the purple colour code in Figure 4-4 for location). The track is ~10 km long with a swath width of ~3 km.

The E-SAR image is significantly brighter in near-range compared to far-range. This incidence angle dependence results from Equation 3.4. Each wind turbine is seen as a bright feature due to direct scattering mechanisms. Very strong scattering, presumably created by a ship, is also observed to the southeast of the wind farm.

5.1 Speckle

The NRCS image in Figure 5-1 has a grainy appearance owing to speckle noise. Speckle is random variation of NRCS, resulting from constructive and destructive interference of the SAR signal caused by different scatterers within each resolution cell (Lewis & Henderson, 1998). Speckle may be reduced through multi-look processing. The SAR bandwidth is partitioned, which leads to a number of independent looks. The looks are combined to form the final SAR image and further smoothing is possible through averaging of pixels in SAR images. Either way, multi-looking causes a decrease of the spatial resolution. The number of statistically independent looks in a SAR image is the equivalent number of looks (ENL). The value of ENL is always less than the specified number of look filters used during image processing (see Section 4). ENL can be computed from image statistics obtained for pixels within a homogeneous area:

$$ENL = \frac{\mu^2}{\sigma^2} \tag{5.1}$$

where μ is the mean value and σ^2 the variance. ENL may then be used to estimate the level of image noise caused by speckle, Q [dB]:

$$Q = 10\log\left(1 \pm \frac{1}{\sqrt{ENL}}\right) \tag{5.2}$$

In case any signal (i.e. true variation of NRCS) is included in the computation of image statistics, the value of ENL will be underestimated and Q will thus be overestimated. Equation 5.2 was used in Paper I for various types of satellite SAR data. Values of Q were ± 0.2-0.3 dB after pixel averaging to 400 m. For the aircraft data, a truly homogeneous area could not be found. The noise level was estimated to be at least ± 0.1 dB for the aircraft data, after pixel averaging to 100 m.

5.2 Ocean scattering

Since the first satellite SAR images became available from SEASAT, it has become evident that many different atmospheric and oceanic features are detectable with a SAR (Fu & Holt, 1982). SAR instruments have been used for detection of wind speed variations related to e.g. atmospheric roll vortices, lee phenomena, and rain cells. Oceanic investigations embrace waves, current fronts, bathymetry, sea ice, and surfactants. Generally, high-frequency radars (X-band) are the most sensitive to wind speed variation, whereas lower frequency instruments (L-band) are more suitable for detection of waves (Schmidt et al., 1995). C-band sensors are responsive to all of these phenomena, which is an advantage in the sense that one instrument may cover a broad range of applications. Discriminating between atmospheric and oceanic features can be difficult in C-band. A multifrequency/multipolarization approach has been suggested for this discrimination (Ufermann & Romeiser, 1999).

6 Wind retrieval from SAR

Capillary and short-gravity waves at the ocean surface are generated by the instant wind. As described above, these waves interact with radar pulses through Bragg scattering; there is thus a relationship between the local wind strength and NRCS. The wind-to-backscatter relation has been empirically established and it generally takes the following form (see also Paper V):

$$\sigma^0 = U^{\gamma(\theta)} A(\theta) \left[1 + B(\theta, U) \cos\phi + C(\theta, U) \cos 2\phi \right] \qquad (6.1)$$

where σ^0 is the normalized radar cross section (NRCS), U is wind speed at the height 10 m, θ is the local incidence angle, and Φ is the wind direction with respect to the radar look direction. A, B, C, and γ are functions of wind speed and the local incidence angle.

A series of geophysical model functions (GMF) have been developed with various coefficients of A, B, C, and γ. Widely used GMFs include CMOD-IFR2 (Quilfen et al., 1998), CMOD4 (Stoffelen & Anderson, 1997), and the more recent CMOD5 (Hersbach, 2003). The GMFs were originally developed for global coverage scatterometer wind retrievals. Scatterometers are capable of 'seeing' the same ground target from different look angles using multiple antennas; therefore a unique relationship exists between σ^0, U, and Φ. The nominal accuracy on wind speed retrievals is ± 2 m s^{-1} and the scatterometer model functions are valid at 2-24 m s^{-1} for incidence angles of 20-60° (Stoffelen & Anderson, 1997). GMFs apply to open oceans with a near-neutral atmospheric stability. Brown (2000a; 2000b) has pointed out a number of potential problems related to the establishment of empirical algorithms from ship and buoy measurements of wind speed. For example, the measurements may suffer from flow distortion or they may have been obtained with non-neutral atmospheric conditions such that an inherent bias is present. These problems are discussed further in Paper III.

GMFs have been applied successfully to wind retrieval from high-resolution SAR imagery; a review is given by Monaldo & Kerbaol (2003). SAR wind retrievals deviate from the scatterometer retrievals in that *i)* SAR images extend to the coastline, and *ii)* several wind speed and direction pairs correspond to a given NRCS because SAR imagery is obtained from only one look direction. It is thus necessary to obtain a priori information on the wind direction to retrieve the wind speed. Methods to retrieve the wind direction are described in Section 6.1. Once the wind direction has been determined, the wind speed may be found from inversion of Equation 6.1. The inversion typically involves the generation of a look-up table or a series of iterations. It is recommended to use pixel averaging to eliminate speckle noise and variations of NRCS due to oceanic parameters (Hasager et al., 2004; Horstmann et al., 2000b). Figure 6-1 shows a wind map generated from an Envisat ASAR scene acquired in wide swath mode over Danish waters.
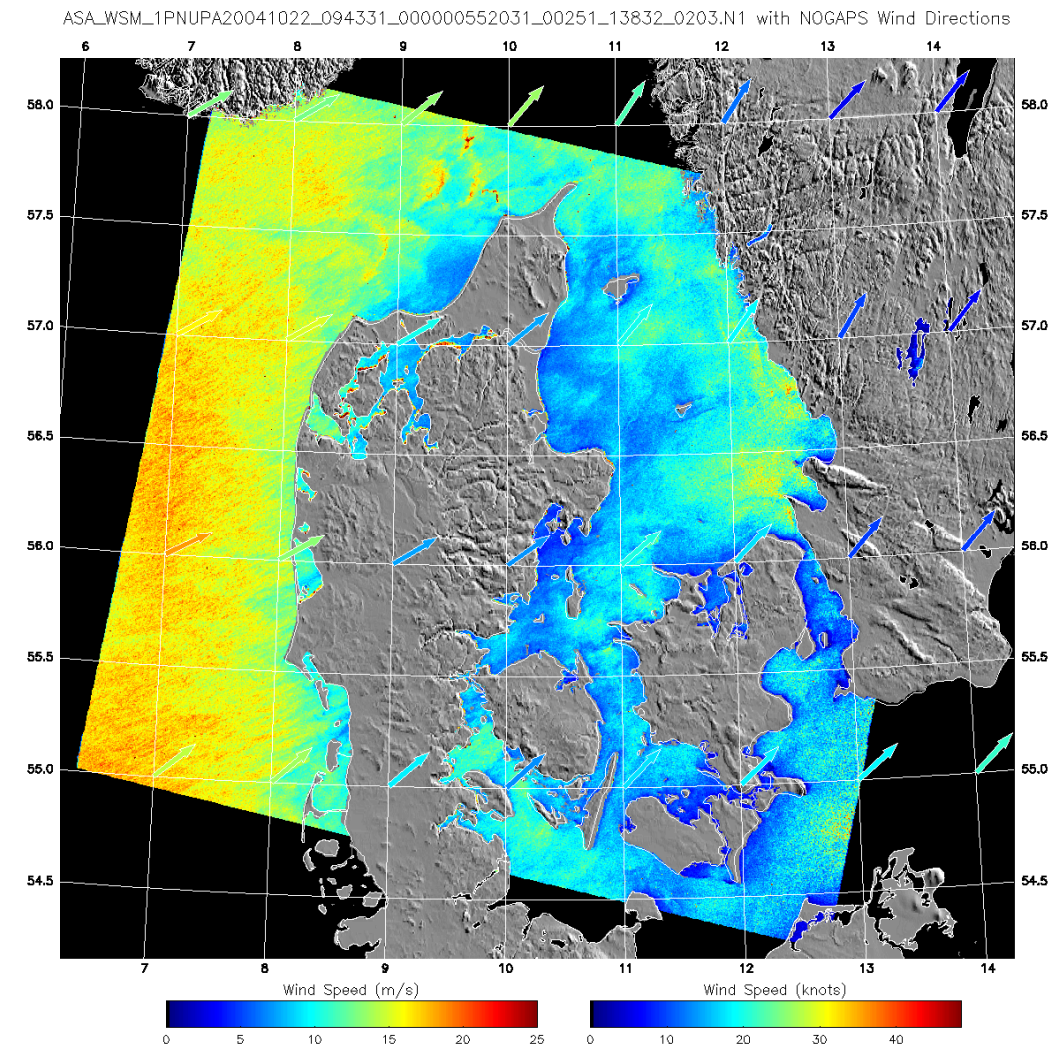
Figure 6-1. Wind field over Denmark from an Envisat ASAR scene acquired 22 October 2004. Arrows represent NOGAPS model winds that correspond well to the alignment of image streaks and to the wind speed retrieved from SAR. Winds were retrieved with the ANSWRS tool (JHU/APL) using the model wind directions as input.

6.1 Determining the wind direction

The wind direction input necessary for SAR wind speed retrievals may be obtained from in situ measurements, if available. This method is very accurate when high quality meteorological data are available and for studies restricted to an area near the meteorological station (e.g. at the Horns Rev wind farm site, see Paper III) As swath widths are now up to 500 km, a wind direction observation from *one* point is generally insufficient for practical wind mapping. In addition, meteorological measurements at offshore locations are sparse and often protected for commercial reasons.

Several methods have been exploited to obtain the wind direction from km-scale streaks in the SAR images, aligned approximately with the wind direction. The streaks originate from atmospheric roll vortices impacting the sea surface. Streak directions have been

resolved with a 180° ambiguity through FFT (Furevik et al., 2002; Gerling, 1986; Lehner et al., 1998; Vachon & Dobson, 1996), wavelet analysis (Du et al., 2002; Fichaux & Ranchin, 2002), and the local gradient method (Horstmann et al., 2002; Koch, 2004). The latter was used for the study presented in Paper III. The major advantage of determining wind directions from image streaks is the exact correlation in time and space between wind speed and direction. A problem associated with the method is the separation of wind-generated streaks from other linear image features (e.g. ice edges, coastlines). As shown in Paper III, this issue causes some uncertainty on fully automated wind direction retrievals. The accuracy on wind directions may improve significantly if directional retrievals are manually supervised, for example by rejection of erroneous wind vectors.

The possibility of obtaining wind directions from scatterometer data has been investigated (He et al., 2005; Monaldo et al., 2004). The method requires nearly simultaneous overpasses of a SAR and scatterometer, which becomes more practical with increasing latitudes. A solution to this time correlation issue, may be a routine merging of the two data types (Monaldo & Beal, 2004).Wind directions extracted from atmospheric models have been successfully applied to SAR wind speed retrievals, despite the need for interpolation in time and space (Monaldo, 2000; Monaldo et al., 2001). As seen in Figure 6-2, it is possible to describe even complex wind direction patterns using model data. Models do sometimes fail to give the correct positioning of e.g. a weather front. This is important at Danish latitudes where the wind climate is dominated by front systems traveling eastward.

6.2 The polarization ratio

The radar return from SAR data in C_{HH} is lower than corresponding returns in C_{VV} for incidence angles above 20° (Paper II). To compensate for the lower NRCS of C_{HH} data, the right-hand side of Equation 6.1 is multiplied with a polarization ratio, *PR*:

$$PR = \frac{\sigma^0_{VV}}{\sigma^0_{HH}} \tag{6.2}$$

where σ^0_{VV} and σ^0_{HH} are the horizontally and vertically polarized NRCS, respectively. The polarization ratio varies with incidence angle and, possibly, with the radar look direction. The relationship is not fully understood, owing partly to calibration errors for the various types of SAR data that have been used to establish *PR*. Definitions of *PR* have been proposed by e.g. Thompson et al. (1998), Vachon & Dobson (2000), and Mouche et al. (2005). In this project, the polarization ratio of Elfouhaily (1996) was used to retrieve winds from the aircraft SAR data acquired in C_{HH}:

$$PR_{Elfouhaily} = \frac{(1 + 2\tan^2\theta)^2}{(1 + 2\sin^2\theta)^2} \tag{6.3}$$

where θ is radar incidence angle (Paper II).

6.3 Wind retrieval software

Several software tools have been developed for SAR wind retrieval. Risø and the Nansen Environmental and Remote Sensing Center (NERSC), Norway, developed the WEMSAR tool in 2000-2003, which handles wind retrieval from calibrated ERS-2 SAR data. Wind directions are obtained from FFT analysis of image features, or from in situ measurements (Furevik et al., 2003; Hasager et al., 2002; 2004).

The GKSS Research Center in Germany has developed the WiSAR tool, which was used for the work presented in Paper III. WiSAR finds the wind direction from local gradient image analysis and performs calibration and wind retrieval for several image types (e.g. ERS-2, Envisat, RADARSAT-1). It works operationally and has been implemented for hurricane tracking (http://w3g.gkss.de/G/Mitarbeiter/horstmann.html/hur_sar.htm) at University of Miami, Florida.
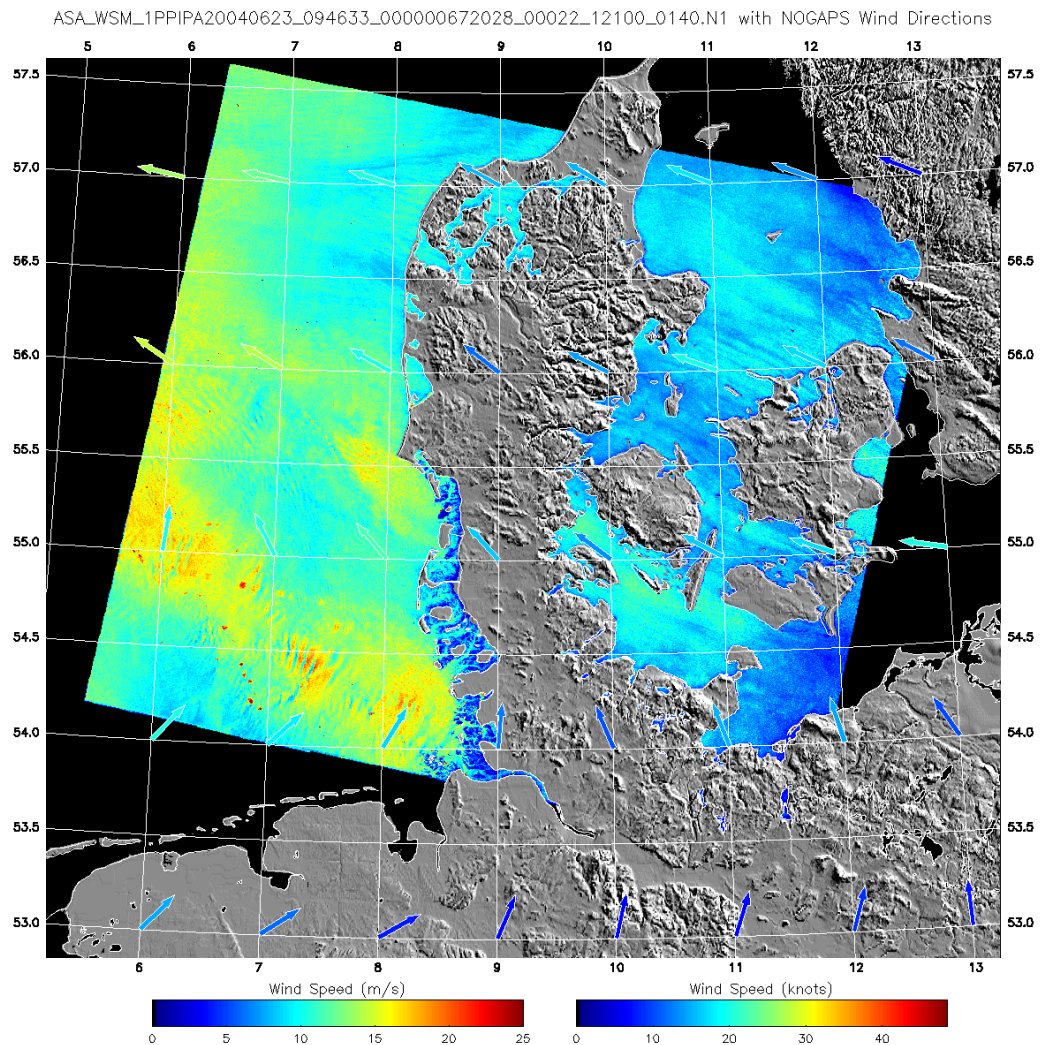

Figure 6-2. Wind field over Denmark from an Envisat ASAR scene acquired 23 June 2004. The wind map shows a complex situation with turning winds in the North Sea. Arrows represent NOGAPS model winds that correspond well to the alignment of image streaks and to the wind speed retrieved from SAR. Winds were retrieved with the ANSWRS tool (JHU/APL) using the model wind directions as input.

At The Johns Hopkins University, Applied Physics Laboratory (JHU/APL), the operational tool ANSWRS enables near real time calibration and wind retrieval from RADARSAT-1 images provided by the Alaska SAR Facility (http://fermi.jhuapl.edu/sar/stormwatch/). Winds may also be retrieved from Envisat ASAR images. The tool uses, as default, wind directions from the NOGAPS model at a 1° latitude/longitude spatial resolution, interpolated in time and space to match the satellite images. The ANSWRS tool was used for the analyses presented in Paper V and VIII, and for retrieval of the wind fields in Figure 6-1 andFigure *6-2*.

A software package is commercially available from French BOOST Technologies (http://www.boost-technologies.com). This package handles all steps in the processing of SAR images to wind maps and users have the opportunity to load wind directions from any source. Finally, numerous tools have been developed for research purposes. For example, the three CMOD algorithms described above were coded in IDL within this project and used for the wake analyses presented in Paper I and II.

6.4 The accuracy of SAR wind retrievals

Numerous comparison studies have been conducted to determine the accuracy of SAR wind retrievals (Furevik et al., 2002; Hasager et al., 2004; Horstmann et al., 2005; Monaldo et al., 2001). Results of these comparisons are summarized in Paper III. Generally, the standard deviation on wind speed retrievals is below ±2 m s^{-1}. This deviation represents the total uncertainty of *i)* NRCS, *ii)* the local incidence angle (θ), and *iii)* the relative wind direction (Φ).

The relative accuracy on NRCS is addressed in Section 5.1 for the data types used in this project. It amounts to ±0.1-0.3 dB after appropriate pixel averaging, which corresponds to wind speed uncertainties below ±1 m s^{-1} (see Paper III, Figure 1). The extraction of spatial wind speed averages, rather than single pixel values, reduces the uncertainty on estimated wind speeds further. The noise equivalent NRCS (i.e. the instrument noise floor) is typically below -20 dB for C-band SARs (Holt, 2004). A threshold wind speed of ~2 m s^{-1} is required for Bragg waves to form and to ensure a signal above the noise floor. SAR scenes with very low wind speeds were therefore disregarded for wind retrieval in this project.

The local incidence angle is usually well determined by SAR processing facilities. The relative wind direction, in contrast, is a major source of error. This is reflected in the above description of methods for determining the wind direction. As illustrated in Paper II (Figure 1), NRCS is least sensitive to wind direction errors when the radar look direction is upwind, downwind, or crosswind. At all other directions, the sensitivity to wind direction increases with incidence angle and wind speed. General estimates of the error on SAR wind retrievals are not easily given, owing to the complex relationship of NRSC, θ, and Φ in Equation 6.1. For a specific wind retrieval, one needs to compute the wind speed sensitivity according to the actual values of Φ and θ. For example, a ±10° error on the relative wind direction (Φ) may lead to an error on wind speed of ±3 m s^{-1} for $\Phi = 45°$, whereas the error is negligible for e.g. $\Phi = 90°$ (for a constant wind speed of 10 m s^{-1} and $\theta = 35°$) (Horstmann et al., 2000a).

Comparison of SAR and in situ winds at Horns Rev
Wind fields were retrieved from a total of 91 ERS-2 SAR and Envisat ASAR images over Horns Rev for the purpose of comparing SAR and in situ winds (Paper III). The wind direction input was obtained from in situ measurements and from local gradients (LG) of

NRCS. The latter was done with the WiSAR tool in collaboration with GKSS. The ambiguity of LG wind directions was resolved through a manual selection of wind vectors, according to visible wind shadows (i.e. lee effects behind obstacles) in the images, and through a fully automatic comparison with model wind directions. Wind speeds were retrieved from CMOD-IFR2, CMOD4, and CMOD5 using the three different wind direction inputs. The mean wind speed was extracted for an area in the vicinity of the meteorological mast using a scalar footprint approach (Gash, 1986), and a simple box averaging method with and without a mask. The mask eliminated areas with a very large gradient of NRCS, presumably caused by other factors than the surface wind. A total of nine estimates of the mean wind speed were available for comparison with in situ measurements.

Wind directions were retrieved with an accuracy of ~20° and ~30° for the supervised and automatic LG method, respectively. In most cases, the automatic retrievals corresponded well to the supervised LG retrievals and to in situ measurements. However, the automatic retrieval failed in a few cases where changing wind directions occurred within one SAR image (e.g. during a front passage). This was mainly due to inaccurate positioning of weather fronts in the temporally interpolated model data.

Figure 6-3 shows the directional distribution of winds for the 91 samples. The in situ data and the supervised LG retrieval show that southeast is the prevailing wind direction with large contributions from the southwest and northwest. The prevalence of southeasterly winds is not repeated for the fully automatic LG retrieval. None of the wind roses reflect the true directional distribution at Horns Rev, as given by time series of meteorological measurements. According to Sommer (2003), the prevailing wind direction is southwest at Horns Rev, whereas contributions from the southeast are relatively small. A solution to this problem may be a weighting of the contribution from each directional sector according to time series measurements (Choisnard et al., 2004).
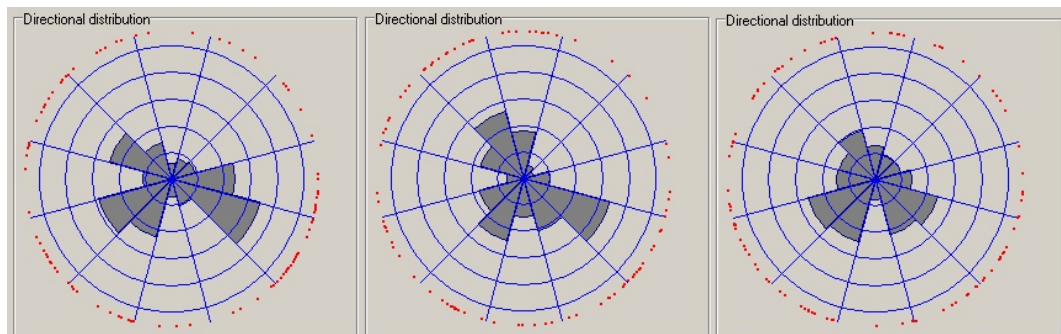
Figure 6-3. Directional distribution of the wind from 91 samples at Horns Rev (samples are shown with red dots). Left: in situ measurements (62 m), center: manually supervised local gradient retrieval, and right: fully automatic local gradient retrieval.

The best approximation of SAR winds speeds to in situ measurements was found for wind retrievals using in situ wind directions. For CMOD-IFR2, a standard deviation of 1.1 m s^{-1} was found with a bias of -0.3 m s^{-1}. CMOD4 showed a numerically larger deviation and bias, whereas CMOD5 was bias-free. The accuracy of CMOD5 wind retrievals was similar to that of CMOD-IFR2, except in the situation of high wind speeds combined with a radar look direction against the wind (see Paper III, Figure 1). The wind retrievals based on CMOD-IFR2 with LG wind directions yielded a standard deviation of 1.4 m s^{-1} for the supervised and 1.7 m s^{-1} for the automatic retrievals.

7 Winds in the marine atmospheric boundary layer

This section begins with a description of important characteristics of the marine atmospheric boundary (MABL). Several properties of MABL must be kept in mind as SAR wind fields are interpreted and used for offshore wind energy applications. These properties include the logarithmic wind profile, internal boundary layers, and atmospheric stability (Garratt, 1992; Stull, 1991). The last four subsections describe atmospheric phenomena causing wind speed variations in the MABL (i.e. convective cells and rolls, lee effects, gap flows, barrier jets, and rain cells) and their signature on SAR imagery. Altogether, processes in the MABL account for the turbulent exchange of momentum, heat, water vapor and other gases between air and sea.

7.1 The logarithmic wind profile

A fundamental assumption in wind retrievals from SAR measurements is that the wind speed increases logarithmically with height. Further, the wind speed at any given height within the MABL is related to the aero-dynamical roughness at the sea surface. This is described by the logarithmic profile law e.g. Stull (1991):

$$u_z = \frac{u*}{\kappa}\left[\ln\left(\frac{z}{z_0}\right) - \Psi_m\left(\frac{z}{L}\right)\right] \tag{7.1}$$

where u is wind speed at the height z, $u*$ is friction velocity, z_0 is the aerodynamic roughness length, and κ is the von Karman constant (0.4). The second term within the square brackets is a stability correction term, where ψ_m is a universal stability function and L is the Obukhov length, determining the atmospheric stability. To compute L, one needs measurements of the vertical heat flux. Such measurements are not available for most offshore applications, therefore neutral atmospheric conditions are often assumed. Alternatively, the bulk Richardson number may be used to determine the dynamic atmospheric stability from simple measurements of temperature and wind speed gradients. This method is described in Section 7.3.

7.2 Internal boundary layers

Internal boundary layers (IBL) develop as wind flow passes over an aerodynamic roughness change, as it takes the flow some time (or distance) to adjust gradually to the new surface properties (Garrat, 1990). The interface between land and sea represents a relatively large roughness change, therefore IBL are common in near-shore areas, where offshore wind farms are operating. With offshore winds, the wind speed measured at some height above the sea surface may correspond to z_0 over land rather than to the smaller z_0 offshore.

Thermal internal boundary layers (TIBL) may develop from temperature changes from land to sea, as land surfaces warm up quicker than the sea. A warm air flow from land will become stably stratified over the sea, as it cools down and gains in density. Further offshore (i.e. beyond 30 km) an inversion lid remains with warm air aloft and cool, well-mixed air near the surface. The layer near the surface has now become near-neutral (Lange et al., 2004a; Lange et al., 2004b). For all IBL examples mentioned here, the logarithmic profile law may fail to predict the wind speed at a given height.

Paper IV (Figure 2) shows how the mean wind speed obtained from 85 SAR scenes increases over a distance of 50 km from the coastline. The application of empirical GMFs for SAR wind retrieval within this near-shore transition zone may be questioned. On the other hand, SAR scenes with onshore and offshore winds showed a similar standard deviation from in situ measurements at Horns Rev, when compared in Paper III. The negative bias, in contrast, was larger for offshore winds.

7.3 Atmospheric stability

Studies of meteorological data from offshore masts in Denmark have shown that non-neutral atmospheric conditions occur frequently, especially at low to moderate wind speeds (Barthelmie & Pryor, 2006; Motta et al., 2005). It is thus important to take stability into account in offshore wind energy studies, whenever possible.

The bulk Richardson number is an approximation to the gradient Richardson number, which determines the buoyant production or consumption of turbulence divided by the shear production of turbulence. The bulk Richardson number was used in this project to determine the atmospheric stability at the times of SAR data acquisition:

$$Ri_B = \frac{g}{T} \frac{\Delta\theta_{Temp} / \Delta z}{(\Delta u / \Delta z)^2} \qquad (7.2)$$

where g is the acceleration due to gravity, T is absolute temperature, θ_{Temp} is potential temperature, and z is height above the surface. The following intervals were defined: Ri_B < -0.4 for unstable atmospheres, $-0.4 \leq Ri_B \leq 0.1$ for near-neutral atmospheres, and Ri_B > 0.1 for stable atmospheres. Stability corrections based on Ri_B have previously shown a deteriorating effect on SAR wind retrievals (Hasager et al., 2004). Values of Ri_B were therefore only used for a grouping of SAR scenes according to atmospheric stability. In Paper III, it was shown that a higher accuracy on SAR wind retrievals can be found for near-neutral conditions compared to unstable and, especially, stable conditions.

Within this project, the potential temperature gradient in Equation 7.2 was based on measurements of air temperatures at two heights. For the measurement campaign at Horns Rev on 12 October 2003, the possibility of using sea surface temperatures (SST) from optical satellite measurements to derive Ri_B was investigated. SST derived from satellite should give the surface skin temperature (i.e. the temperature within the uppermost millimeters of water). The SST map in Figure 7-1 is based on a MODIS Aqua product (see Section 4.3 for product specifications). At Horns Rev, an SST of 13-14°C was found from the map, which corresponded well to in situ measurements at -4 m water depth (13.7 °C). The air temperature was 12.5 °C at 13 m, in agreement with measurements from other Danish stations (i.e. Høvsøre and Børglum, see Paper II). The resulting Ri_B suggested strongly unstable conditions. In contrast, direct measurements at Høvsøre to the north of Horns Rev showed a very small negative temperature gradient, leading to a Ri_B of -0.1 and near-neutral conditions. The combination of satellite SST and in situ air temperature measurements was found to be too uncertain for stability classification in this project. Having said that, there may be other benefits related to the use of optical SST images in combination with SAR data. Thompson et al. (2004) have shown a striking correlation between NRCS from SAR images and SST from the optical NOAA AVHRR sensor with stable atmospheric conditions. This confirms the dependency of surface wind stress (and thus NRCS) on atmospheric stability.
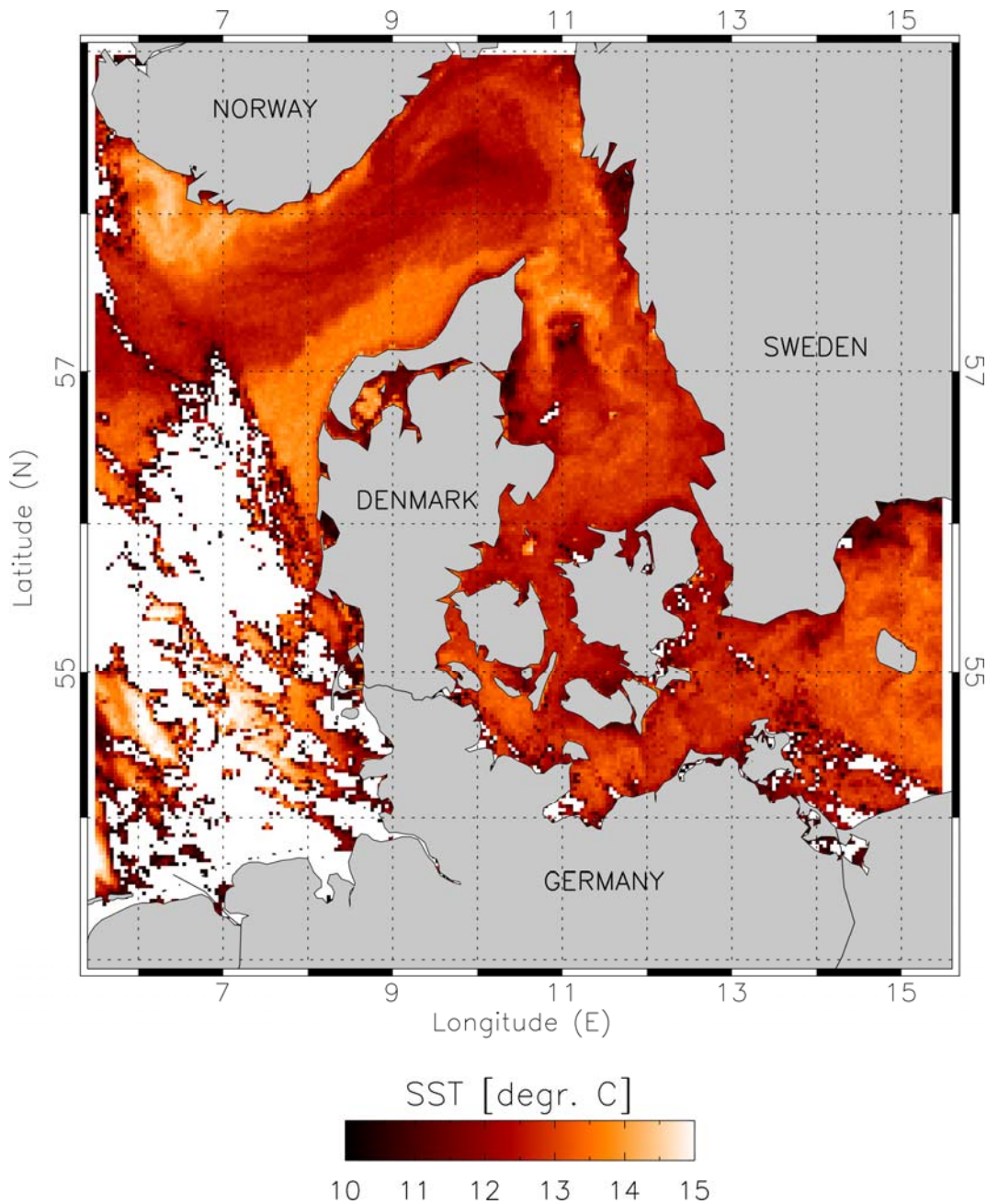
Figure 7-1. MODIS image showing sea surface temperatures (SST), 12 October 2003 at 11:50 UTC. White areas are cloud covered. SST at Horns Rev is 13-14° C, corresponding well to the measured temperature at water depth -4 m (13.7° C).

7.4 Convective cells and roll vortices

Convective cells originate at low wind speeds from a negative air-sea temperature difference (i.e. a warm sea and cooler air directly above the sea surface). Cell circulation is generated by buoyant updraft and downdraft at scales of one to tens of kilometers. At the sea surface, cell winds are directed either towards an updraft or away from a downdraft. The cell wind direction, with respect to the ambient surface wind direction,

determines the effective wind speed. When the winds are from the same direction, wind speed increases, whereas opposing wind directions lead to a decrease of speed. As the surface wind speed determines the Bragg wave amplitude, convective cells appear as circular patterns of high and low NRSC in SAR images (Sikora & Ufermann, 2004).

At higher wind speeds, a combination of buoyancy and wind shear leads to longitudinal roll vortices aligned approximately with the wind direction. The ratio of buoyancy to wind shear, that determines the development of cells or rolls, is not well defined (Young et al., 2002). Rolls are generated from updraft and downdraft, as described for convective cells. Roll vortices impact the sea surface roughness and are thus visible as linear features in SAR imagery. The spatial scale of rolls is one to tens of kilometers perpendicular to the wind direction. In Section 6.1, methods to retrieve the surface wind direction from roll vortices in SAR images were described.

Roll vortices have also been utilized to determine the depth of MABL assuming that the wavelength of rolls, determined from spectral analysis, corresponds to 1.5 times the boundary-layer depth (Young et al., 2000; Young, 2000). The approach is based on mixed-layer similarity theory (e.g. Stull (1991)) and applies to unstable atmospheric conditions only. Sikora & Thompson (2002) have taken this approach one step further and used the SAR-retrieved depth of MABL to determine the stability parameter z/L in Equation 7.1. A major source of error related to determining the MABL depth from SAR imagery is the choice of pixel averaging. Ideally, a spatial resolution on the order of 100 m is needed to distinguish boundary layer rolls. However, a large amount of speckle noise may still be present at this resolution. Finally, as boundary layer rolls occur approximately 50% of the time for the world's oceans, their influence may be inherent in the empirical GMFs used for SAR wind retrieval (Brown, 2002).

7.5 Lee phenomena

Different flow patterns are associated with wind flow around obstacles. A description of these phenomena is relevant here because they may also occur on the lee side of large offshore wind farms (see Section 9).

Weak wakes
Simple reductions of the mean wind speed downstream of mountains and islands have been detected from numerous SAR-retrieved wind maps e.g. Young & Winstead (2005). The phenomena are referred to as *weak wakes* because the requirements for their development are often and easily met. Wakes can persist over downstream distances of hundreds of kilometers, especially in highly stratified atmospheric boundary layers. Similar phenomena were detected in this project in the form of wind farm wake effects over distances up to 20 km (Figure 9-3).

Atmospheric vortex streets
Von Karman vortex streets are rather complex patterns of wind speed variation on the lee side of obstacles. They have been observed from SAR imagery on the lee side of islands with typical width-to-wavelength ratios around 0.4 (Li et al., 2000; Li, 2004). The phenomenon was not observed on any of the SAR images studied in this project. Numerical simulations have shown that the tips of wind turbine blades in operation do create vortex shedding up to seven rotor diameters downstream of the turbine (Troldborg et al., 2006). The scale of vortices is typically on the order of the obstacle diameter, which is small for wind turbines compared to the spatial resolution of the SAR images studied here. The chance of detecting the vortices was thus limited.

Atmospheric gravity waves

Atmospheric gravity waves (also known as internal waves) develop in stably stratified boundary layers. When air particles pass over an obstacle and are removed from their equilibrium state, waves are generated by buoyancy force. The waves may be oriented perpendicular to the wind direction (transverse waves), or outwards from the wake (diverging waves). The alternating wind speeds associated with atmospheric gravity waves are visible on SAR images and have km-scale wavelengths. Apart from mountains and islands, an offshore platform has been shown to cause atmospheric gravity waves (Chunchuzov et al., 2000). Some of the SAR images studied here (e.g. Paper III, Figure 3) showed features that were interpreted as atmospheric gravity waves generated by the land.

7.6 Gap flows and barrier jets

In Paper V, examples are shown of flow acceleration through mountain gaps (i.e. gap flows). Other examples show acceleration of wind flow as it is diverted by steep obstacles such as coastal cliffs (i.e. barrier jets). A detailed description on how these phenomena form is given in the paper. The site studied was the Gulf of Alaska, which provided very fine examples of gap flows and barrier jets owing to the complex terrain and high wind speeds. Barrier jets have also been observed at other locations e.g. along the US west coast. Knowledge about gap flows and barrier jets, obtained from SAR imagery, has an obvious value in offshore wind farming: the positioning of wind farms relative to these phenomena is crucial for power production and fatigue loading. In addition, SAR wind maps quantifying the effect of complex terrain is useful for validation of mesoscale models and for a range of meteorological applications.

7.7 Rain cells

C-band SAR instruments are generally capable of penetrating rain clouds in the atmosphere. However, rain cells may still be visible in SAR images owing to two types of impact on the sea surface roughness. The first is impinging of raindrops at the surface, which enhances or decreases the Bragg wave amplitude, depending on the rain rate (Melsheimer et al., 1998). The second impact is associated with wind gusts. Rain cells are characterized by a strong downdraft at their core where the limited horizontal wind shear leads to a reduction of NRCS (Atlas, 1994). As the downdraft spreads in all directions, the surface stress increases. At low ambient wind speeds, the spreading results in circular cell signatures in SAR images. Higher wind speeds lead to more elongated signatures. Rain cells usually have a sharp edge called a gust front. Rain cell signatures in a SAR image are depicted in Figure 7-2; other examples have been given by Alpers & Melsheimer (2004).
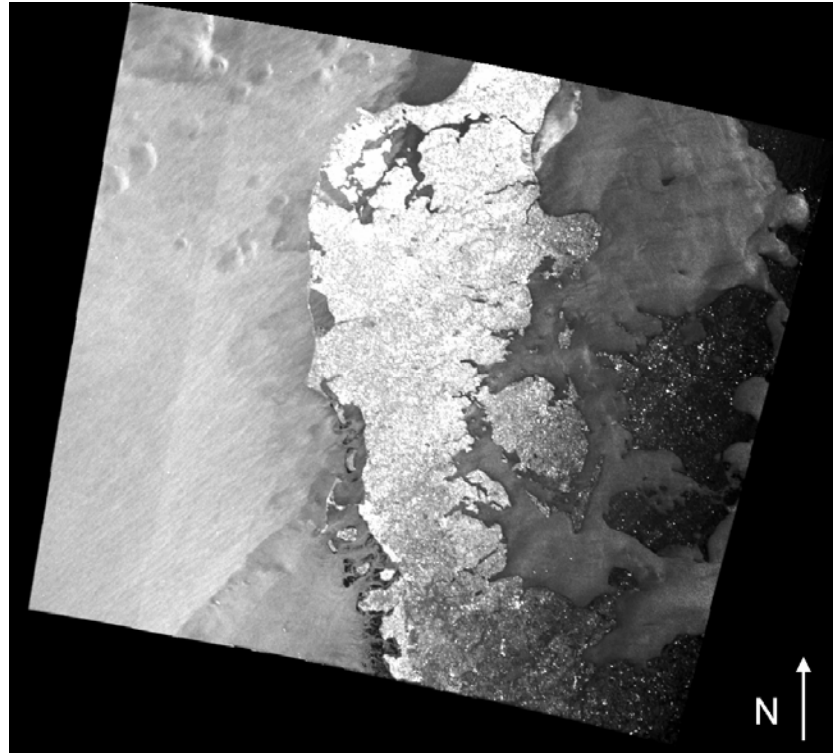
Figure 7-2. Envisat ASAR scene acquired in wide swath mode over Denmark on 6 October 2004. Coverage 400 km x 400 km. Rain cells are seen in the North Sea (upper left corner). Note also the atmospheric roll vortices (i.e. wind streaks) in the North Sea indicating a wind direction of ~220° in agreement with mast measurements at Horns Rev.

8 Oceanic influences on SAR measurements

This project is concerned with atmospheric parameters and ocean winds in particular, as measured from C-band SAR. During the analysis of SAR scenes within the project, it became clear that oceanic parameters impact SAR wind retrievals through the complex interaction of air and sea. In the following, a brief description of the relevant oceanic parameters is given with examples from the analyzed data set. The oceanic parameters are typically seen on SAR images acquired at low wind speeds. As the wind speed increases, the wind becomes the dominating parameter in determining the amplitude of Bragg waves.

8.1 Surface waves

On the aircraft SAR image shown in Figure 5-1, periodic surface waves aligned diagonal to the flight direction are visible, thanks to the high spatial resolution. Surface waves are typically 100-600 m long and wind-generated (Vachon et al., 2004). They propagate as swell from the region of origin and brake as they approach shallow waters. The alternating NRCS, observed for the wave crests and troughs, result from tilt and hydrodynamic modulation (Alpers et al., 1981; Hasselmann et al., 1985). Tilt modulation is caused by variation in the local incidence angle, as Bragg waves ride on longer period waves. Hydrodynamic modulation refers to a modification of the Bragg wavelength and amplitude by the long period waves. Bragg waves are typically shorter at the crest of surface waves compared to the trough. Tilt and hydrodynamic modulation is particularly strong when surface waves are traveling directly towards or away from the radar. In addition, long period waves (and other objects) may cause image distortion when propagating in the azimuth direction, owing to changes in the Doppler shift. This distortion is called velocity bunching.

The length of the surface waves visible in the aircraft SAR images (Figure 5-1) was estimated to ~100 m through spectral analysis. To average out the wave modulation from surface waves, pixels were averaged to a size of 100 m for the E-SAR wind mapping. From Figure 5-1 it is evident that the surface wave alignment is disturbed in the near vicinity of the wind farm due to wave refraction around each of the turbine towers. The towers were assumed to only affect the longer period waves, which were eliminated through the pixel averaging.

8.2 Internal waves

Internal waves propagate within the interior of the ocean and originate from gradients of water density (i.e. pycnoclines). The gradients may result from heating of the surface layer or outflow of low salinity water to the sea. Wave propagation is often triggered by tidal motion. Internal waves have wavelengths of 0.1 to 20 km and travel in groups (Apel, 2004). Internal waves leave a signature in SAR images through modulation of Bragg waves at the sea surface. Roughening of the sea surface occurs for convergent flow and damping for divergent flow, as the orbital motion of internal waves cause interaction with surface currents and waves.

8.3 Currents and bathymetry

Current patterns in near-shore areas are complex as frequent changes of the current direction and magnitude occur over small spatial scales. Examples of near-shore currents include tidal currents, rip currents, and undertow. Currents leave a signature on SAR images when there is a gradient causing flow convergence or divergence (Johannessen et al., 1996; Lyzenga, 1991). For example, the amplitude of a Bragg wave will increase as the wave enters a current field directed opposite the direction of wave propagation. This leads to an increase of NRCS. The amplitude will relax again as the Bragg wave has crossed the current front, therefore fronts appear as narrow features in SAR images.

Strong current gradients may occur as currents pass over bathymetric features e.g. tidal flats, sand bars or submerged reefs. The presence of such bed forms causes the flow to converge. As for other currents, flow convergence leads to an enhancement of small scale surface roughness and an increase of NRCS in SAR images. Flow divergence, in contrast, leads to a reduction of the surface roughness and NRCS. A large effort has been put into modeling the complex interaction of bathymetry, currents, oceanic waves and electromagnetic waves (Alpers & Hennings, 1984; Romeiser & Alpers, 1997) with the ultimate goal of using SAR measurements for detailed bathymetric mapping (Alpers et al., 2004).

The bathymetry issue is very relevant in terms of wind energy studies from SAR, as offshore wind farms are generally built at shallow water depths. Effects of the submerged reef at Horns Rev are discussed in paper I and II. An example SAR image showed a precise outline of the reef, when compared to a bathymetric map (Paper I, Figure 4 and 5). The reef signature was assumed to originate from current/wave interaction or wave breaking. As a rule of thumb, waves break when the ratio of the wave height to the water depth is 0.3-0.8. For the water depth 5 m, waves must be 1.5-4 m high to reach this breaking criteria. The average significant wave height is ~1 m at Horns Rev but wave heights up to 4.3 m occur (Sommer, 2003). Breaking is therefore possible. The presence of wind turbine towers leads to convergence and divergence of current streamlines, analogous to bathymetry effects. Since the tower diameter is small (~5 m) relative to the distance between individual turbines (~500 m), and no tower effects were visible in the SAR images, the tower-current interaction was considered negligible here.

8.4 Surface slicks

Surfactants may be anthropogenic in the form of mineral oil spills or naturally produced by marine plants and animals (i.e. biogenic slicks). Both types of surface slicks have a damping effect on Bragg waves as they float on the sea surface, thus they appear dark on SAR images. This damping mechanism has been utilized in the detection of oil pollution from ships using both satellite (Gade & Alpers, 1999), space shuttle (Gade et al., 1998c) and airborne (Wismann et al., 1998) SAR. Further, controlled experiments have been carried out in the North Sea with various types of surfactants and a helicopter-mounted scatterometer (Gade et al., 1998d). The damping ratio of surfactants has also been investigated through wind-wave tank experiments (Gade et al., 1998b; Gade et al., 1998a).

None of the SAR scenes investigated here showed evidence of mineral oil spills. Biogenic films were observed for three of the satellite scenes acquired over Horns Rev. The scenes were from the spring and summer seasons, when phytoplankton blooms occur (Espedal et al., 1996; Espedal et al., 1998). The SAR image in Figure 8-1 shows the

effect of surface slicks. The bright and dark patterns originate from surface currents that become traceable owing to the accumulation of surfactants in convergent zones. None of the SAR scenes acquired over Nysted showed surfactants. However, a very extensive coverage of biogenic slicks has previously been detected in the Baltic, including the Nysted site, by Alpers & Espedal (2004).
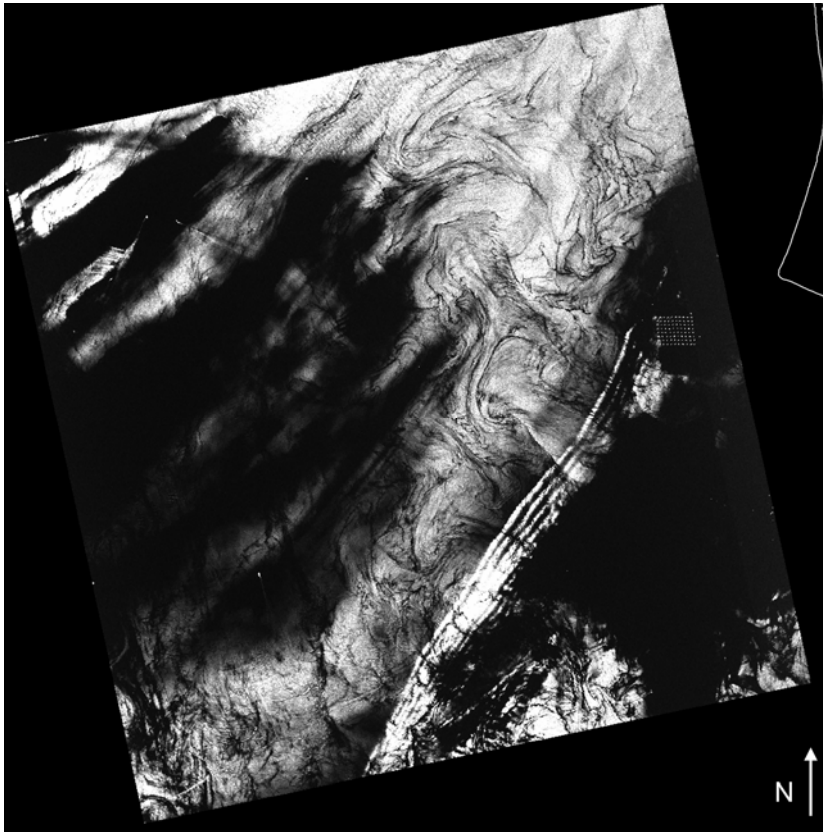
Figure 8-1. ERS-2 SAR scene acquired over Horns Rev on 29 May 2003 at low wind speed (1.8 m s^{-1} from mast). Coverage 100 km x 100 km. Current patterns are traceable owing to surface slicks; and the wind turbine array is visible. Parallel bright bands may result from atmospheric internal waves. Wind direction: 330° from mast.

The very noticeable bright bands in Figure 8-1 are interpreted as atmospheric internal waves, as they are aligned perpendicular to the wind direction (330° from mast) with highly stable atmospheric stratification according to Ri_B. However, no obstacle is present windward of the wave crests to initiate the wave motion. This example illustrates how the interpretation of features seen in SAR images can be difficult.

9 Wind farm wake effects

Wakes are regions of reduced wind speed and enhanced turbulence that are present downstream of any obstacle exposed to wind flow. The extraction of kinetic energy, performed by rotating wind turbines, leads to a further enhancement of the wake effect. Information about individual wakes and their interaction within wind farms is valuable for designing the optimum layout of turbines within offshore wind farms. In terms of large scale offshore wind farming, studies of the wake effect are also relevant for environmental impact assessment and for the optimum siting of wind farms in clusters. Benefits of clustering include the possibility of sharing cables and maintenance costs. However, the wind farm wake effect must be carefully considered to limit wind farm shadowing. This is particularly important when individual wind farms have different operators, as it is the case for the proposed wind farm clusters at Horns Rev and, possibly, at Nysted.

9.1 Wake characteristics

Wind turbines start operating at a cut-in wind speed of ~4 m s^{-1} with an increasing power output up to the nominal wind speed of ~15 m s^{-1}. The power production is kept constant at higher winds to reduce fatigue loading. At the cut-out wind speed of ~25 m s^{-1}, turbines are shut down for safety. Some important characteristics of wind farm wake effects can be seen from Figure 9-1, which is based on production data from the wind farm at Horns Rev, released by Elsam A/S. The production data cover the period from 01/01/2005 to 31/07/2005. For the purpose of this study, data were extracted for one row of turbines (ten in total) at the wind direction 270±15°. Wind speeds covered the interval 4-15 m s^{-1} in 1 m s^{-1} bins. The power ratio was set to 100% for the westernmost turbine (1) and data were only included if all turbines were running. The extracted data set illustrates the maximum possible wake loss, as turbines are perfectly aligned and the investigated turbines are located 'deep' inside the wind farm (Barthelmie et al., 2006).

For wind speeds of 4-10 m s^{-1}, a significant power loss is seen from turbine 1 to turbine 2 (Figure 9-1). The power ratio continues to decrease through the wind farm to a minimum of 55% for turbine 10 at 5 m s^{-1}. The power loss is smaller for wind speeds above 11 m s^{-1}. At 15 m s^{-1}, the power ratio for turbine 1 and 2 is equal (100%) because a sufficient amount of energy is available to keep both turbines running at full capacity. The power production data suggest that wind farm wakes are best studied for wind speeds of 4-10 m s^{-1}.

Figure 9-2 is based on the same data set as Figure 9-1, except power ratios are replaced with velocity deficits obtained from wind speed measurements at the top of each wind turbine hub. The wind speed measurements may be distorted by turbine motion or otherwise biased. This is reflected in the data for turbine 4 and 6, showing smaller deficits than their neighboring turbines. However, the computed velocity deficits provide a basis for direct comparison with results obtained from SAR measurements (see Section 9.4). Velocity deficits were computed according to the procedure used in Paper I and II:

$$VD = \frac{U_{free\,stream} - U_{wake}}{U_{free\,stream}} 100\%$$ (9.1)
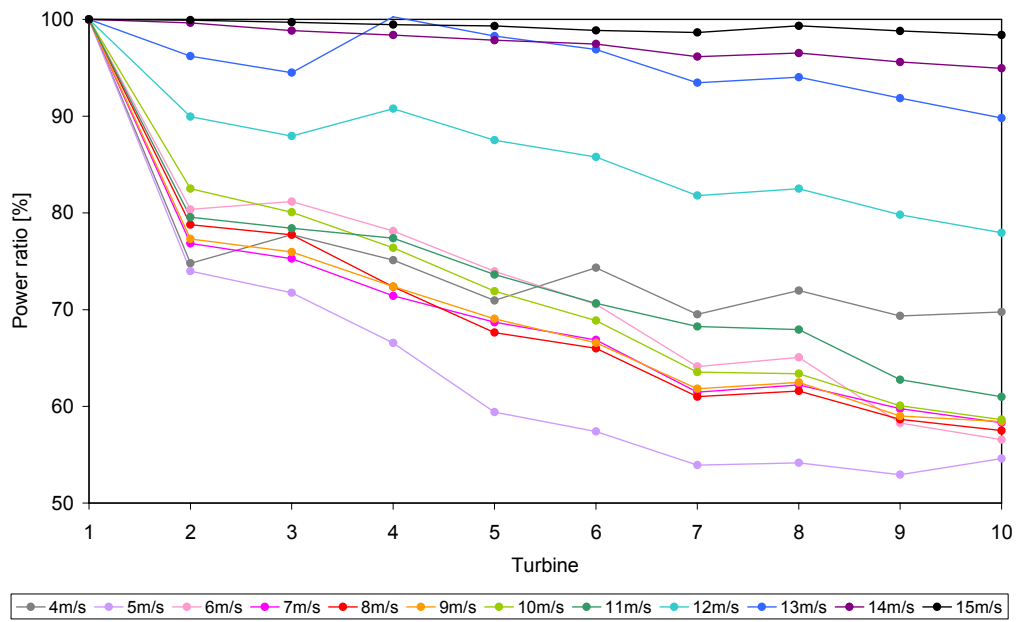
Figure 9-1. Power ratio along one row (west to east) of wind turbines at Horns Rev for wind directions of 270±15°. The power output is set to 100% for the westernmost turbine (1), which is exposed to the ambient flow. The number of samples per wind speed bin varies from 80 to 254, obtained from 01/01/2005 to 31/07/2005 with all turbines in operation (data from Scadaview, courtesy Elsam A/S).

Figure 9-2. Velocity deficit along one row (west to east) of wind turbines at Horns Rev for wind directions of 270°±15°. The deficit is 0% for the westernmost turbine (1), which is exposed to the ambient flow. The number of samples per wind speed bin varies from 80 to 254, obtained from 01/01/2005 to 31/07/2005 with all turbines in operation (data from Scadaview, courtesy Elsam A/S).
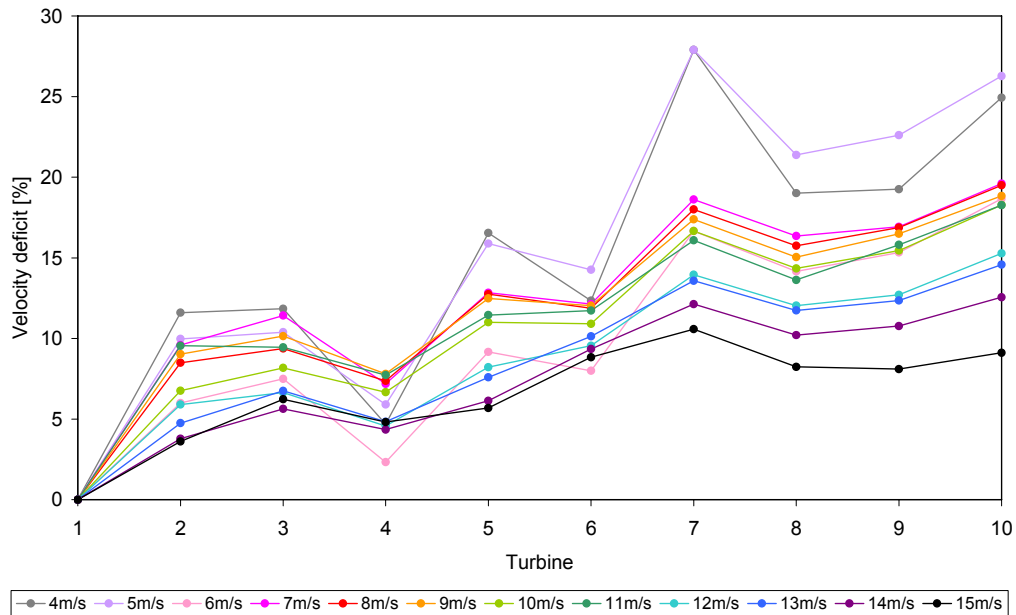
where VD (%) is the velocity deficit, $U_{free\ stream}$ is wind speed in the ambient wind flow (in this case at turbine 1) and U_{wake} is wind speed obtained in the wake (i.e. for any given turbine along the row).

Figure 9-2 corresponds to Figure 9-1 in the sense that the maximum wake effects occurs for the wind speed 5 m s^{-1} with a velocity deficit of ~25% at turbine 10. As for the power ratio, the threshold wind speed for very significant wake effects seems to be between 10 and 11 m s^{-1}. At higher wind speeds, the velocity deficit is below 15%. A velocity deficit remains even at high wind speeds. For example, the velocity deficit at turbine 10 is ~8% at 15 m s^{-1}. It should thus be possible to detect a velocity deficit from SAR wind fields within the range of 4-15 m s^{-1}, despite the power 'saturation' for winds above 10 m s^{-1}.

9.2 Wake modeling

The problem of describing wind farm wakes has been addressed through modeling efforts; a review on wake modeling is provided by (Crespo et al., 1999). The Wind Atlas Analysis and Application Program (WAsP, see Section 10.1) contains the simple wake model PARK, which determines the wake loss downstream of wind turbines. PARK has limitations concerning the wake overlap, which occurs within large offshore wind farms, and it does not take feed-back mechanisms between wakes and the atmospheric boundary layer into account. An analytical model complex has been developed at Risø, which describes individual wakes and their interaction within large wind farms more accurately (Frandsen et al., 2006; Frandsen, 2006). This model is restricted to straight rows of turbines with a uniform spacing but a recent improvement has been proposed, which handles irregular wind farm lay-outs (Rathmann et al., 2006). The analytical model complex was developed mainly for the prediction of power production and design loads within a farm, as part of the project STORPARK (2002-2004). It has not yet been extended to the area downstream of large wind farms.

Wake propagation at larger distances downstream of offshore wind farms has been addressed using the WAsP-PARK model and from an alternative 'added roughness' approach (Barthelmie et al., 2004b; Barthelmie & Pryor, 2006). The former models the momentum deficit caused by wind turbines based on a wake decay constant. The latter approach considers a wind farm as a surface roughness element, analogous to a group of trees. Uncertainty is related to the roughness representation of wind farms and it is also unclear whether the roughness should be re-set immediately downstream of the wind farm or allowed to decay over a longer distance. Wake recovery distances, determined from the 'added roughness' approach with different roughness settings, are 5-14 km (Barthelmie et al., 2004b; Barthelmie & Pryor, 2006).

9.3 Wake measurements

In situ measurements describing the wind farm wake phenomenon are limited. Meteorological masts are costly offshore and a further limitation is the necessity of the masts to be located directly downstream of a given wind farm to capture the wake effect. In the ENDOW project (1999-2001), a wake database was set up for the wind farms at Vindeby, Horns Rev and Bockstigen in Sweden, using measurements from nearby onshore and offshore masts (Barthelmie et al., 2003a; 2004a). Measurements have also been carried out from a ship using sonic detection and ranging (SODAR) (Barthelmie et al., 2003b; Folkerts et al., 2001). In both cases, measurements were restricted to relatively short distances downstream of the wind farm with the primary purpose of

validating wake models for individual turbines. Two meteorological towers have been erected to the east of the wind farm at Horns Rev to obtain wake measurements. At Nysted, a configuration of four masts measure wakes at different wind directions. These data are, like most measurements at wind farm sites, protected for commercial reasons.

9.4 Wake studies using SAR

In the Ph.D. project, SAR wind fields were utilized to study wake effects downstream of the wind farms at Horns Rev and Nysted. The key assumption in the work was that turbine wakes are detectable in SAR imagery, as individual wakes impact the sea surface at a downstream distance of ~10 rotor diameters. Focus was on wake propagation downstream of the large offshore wind farms, as the area with turbines was affected by direct scattering. Of the two parameters characteristic for wakes (i.e. wind speed reduction and turbulence enhancement), emphasis was put on describing variations of the mean wind speed from satellite and aircraft SAR measurements (Paper I and II). Turbulence was addressed briefly (Paper I), as was a comparison of results from SAR and the 'added roughness' model (Paper IV). Applied methods and major findings of the wake study are summarized in the following.

A series of 41 satellite SAR images acquired over Horns Rev and Nysted were analyzed for wind farm wake effects (Paper I). Through visual inspection of the scenes, it soon became clear that some were unsuitable for the wake study. Reasons for eliminating the scenes included various atmospheric and oceanic impacts, most importantly effects of the bathymetry at Horns Rev. On some SAR wind maps, a reduction of the mean wind speed was clearly visible downstream of the wind farms (Figure 9-3). In other cases, wakes were detected as mean winds were plotted along transects crossing the wind farms (Paper V, VII and VIII).

Velocity deficit
To describe wakes in relative terms, velocity deficits were computed (Equation 9.1). A major advantage of SAR measurements was the opportunity to obtain reference measurements along parallel transects, taking the ambient variation of wind speed into account. This was particularly important when winds came from the land such that flow acceleration occurred (Paper IV, Figure 2). A limitation of the parallel transects was that velocity deficits were possible upstream of the wind farm due to wind speed variations in the ambient flow. Velocity deficits found immediately downstream of the wind farms were 8-9% on average. The distance over which the wind speed recovered to match the free stream conditions was 5-20 km and possibly longer for some scenes. Variability occurred from scene to scene, as the persistency of wind wakes was dependent on the ambient wind speed, the atmospheric stability and the number of turbines in operation.

The airborne SAR data from Horns Rev also showed a velocity deficit downstream of the wind farm. Since the SAR data acquisition was restricted to the wake region, the measured wind speeds were normalized with in situ measurements obtained upstream of the wind farm. Velocity deficits up to 20% were found from the aircraft measurements. An ERS-2 satellite SAR scene acquired almost simultaneously suggested a maximum deficit around 10%, as winds in the wake region were normalized with measurements along a parallel transect. This demonstrated how the reference method is crucial for estimates of the wake deficit. Figure 9-2 suggests that the maximum velocity deficit is ~17% at 8-10 m s^{-1} for the wind farm at Horns Rev. This supports results from the satellite SAR images, which were acquired at a wind direction diagonal to the turbine rows.
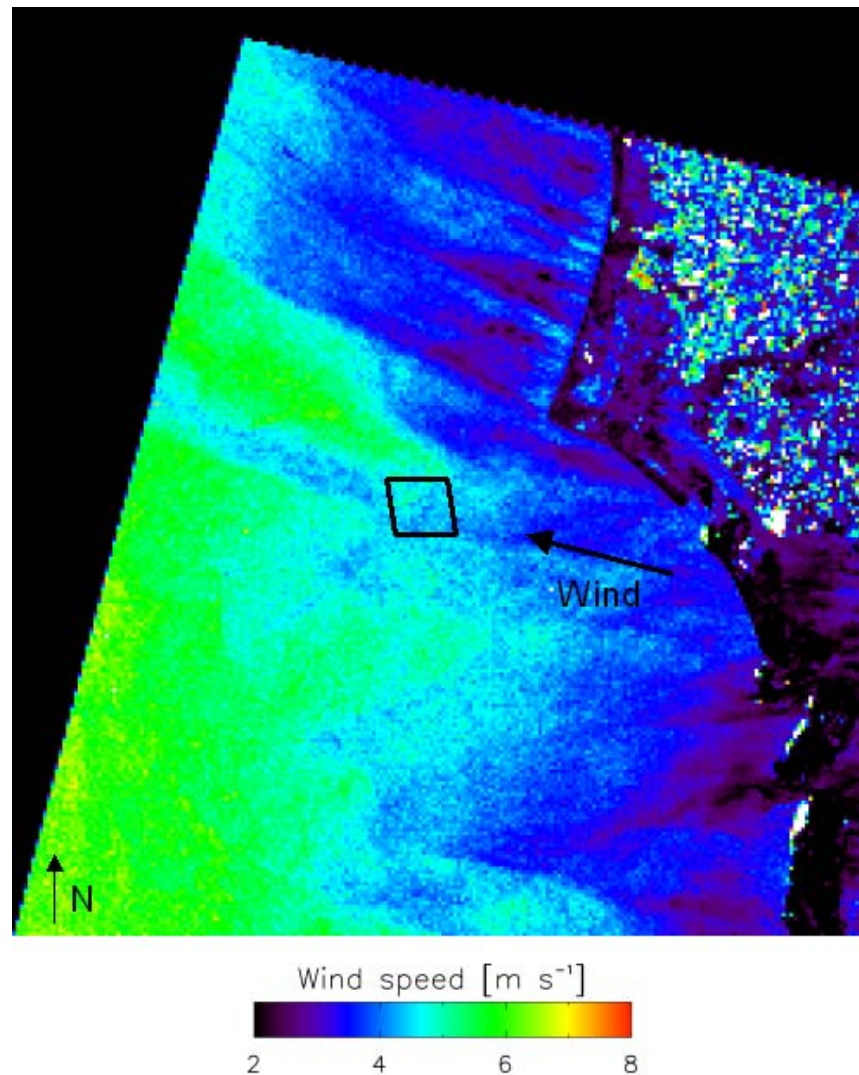
Figure 9-3. Wind field at Horns Rev based on ERS-2 SAR image from 25 February 2003. The black trapezoid indicates the wind farm. For scaling, the total wind farm width is ~5 km. The wind direction is 110° from the meteorological mast. A reduction of wind speed is seen downstream of the wind farm. Note also the strong shadowing effects of the land.

Turbulence

A simple analysis was carried out to identify regions of enhanced turbulence intensity downstream of the wind farms at Horns Rev and Nysted. The analysis followed the basic assumption that added turbulence should lead to an increased standard deviation of SAR-retrieved wind speeds. Ambient turbulent length scales offshore have been estimated to peak around 500 m (Petersen et al., 1998), which is on the same order as the spatial resolution of satellite wind maps. The scale of turbulence is typically reduced in the lower wake (i.e. below turbine hub-height) compared to the ambient flow (Højstrup, 1999). An enhancement of the turbulence intensity was found for 50% of the cases studied. The ambiguity may result from a lack of turbine generated turbulence near the sea surface, as found through measurements by Frandsen & Christensen (1994). It is also possible that turbulence persisted at the sea surface but was non-detectable from the SAR imagery due to deviations in scale.

Comparison of SAR and wake model results

SAR winds were compared to results from the 'added roughness' wake model for a test case from Horns Rev (Paper IV). The model was run with a free stream velocity obtained from the SAR image and a surface roughness derived indirectly form the SAR measurements using Charnock's equation (Charnock, 1955) combined with the logarithmic profile law downstream of the wind farm. Once the surface roughness is determined, wind speed can be modeled at any height. Here, the wind speed at 10 m and at hub-height were predicted. The model predicted a wind speed recovery to the free stream velocity after 9 km and the SAR measurements indicated a slightly faster recovery. A possible explanation may be the model assumption that all turbines were running, which may not have been the case.

The comparison illustrates how SAR measurements may be useful in determining the behavior of surface roughness downstream of wind farms. The information is useful in the tuning of 'added roughness' wake models. Note that the method used for comparison assumes a logarithmic increase of wind speed with height, which may not be the case in the wake of large wind farms. On the other hand, the validation study described in Paper III showed a good agreement of SAR and in situ winds in the wake of the wind farm at Horns Rev. The wake impact on vertical wind profiles may thus be comparable in magnitude to atmospheric stability effects.

9.5 Key results on wind farm wake effects

The following conclusions were drawn, based on the study of wind farm wake effects from SAR measurements:

- SAR wind fields (both satellite and airborne) are useful for describing the spatial variability of wind speed caused by wind farm wakes.
- The wake extent and magnitude depend on the ambient wind speed, the atmospheric stability, and to a certain threshold on the number of turbines in operation.
- Offshore wind farm wakes may extend over very long distances (i.e. beyond 20 km downstream of wind farms).
- Velocity deficits are typically 10-20% in the near-vicinity of large offshore wind farms.
- Turbine-generated turbulence may not be detectable from the standard deviation of SAR wind fields.

10 Wind resource assessment

10.1 The WAsP principle

Accurate assessment of the wind resource is crucial in the planning and bidding phase of new wind farm projects. Long-term experience in the field of wind resource assessment has been gained at Risø through development of the Wind Atlas Analysis and Application Program (WAsP) (Mortensen et al., 2005; Troen & Petersen, 1989). WAsP relies on statistical analyses of wind speed and direction measured at meteorological stations. Weibull functions are fitted to the measured wind speed for a number of wind direction sectors. A Weibull distribution is characterized by a shape (k) and a scale (A) parameter, necessary for prediction of the wind power density.

Fundamentally, a suite of WAsP models allow for removal of local and regional effects (i.e. sheltering obstacles, terrain roughness, and topography), which leads to a generalized wind climate. A wind atlas over Europe has been published on the basis of generalized wind climates (Troen & Petersen, 1989). National wind atlases have been generated for more than 30 countries (see www.wasp.dk and www.windatlas.dk); the most recent atlas covers Egypt (Mortensen et al., 2006). In order to predict the wind resource at a given location, local and regional effects for that specific location must be added to the generalized wind climate. Information about sheltering obstacles, terrain roughness, and topography are usually obtained from field trips, land use maps, topographic maps, or satellite images. The accuracy of wind resource assessment depends on the quality of meteorological measurements and on the similarity between the meteorological station and the site subject to investigation. Basic requirements include at least one year of continuous measurements as well as similar topographic settings and climatic conditions.

10.2 Wind resource assessment from SAR

In the offshore environment, where in situ measurements are sparse, SAR wind fields have proven useful for wind resource assessment (Paper IV and Hasager et al. (2005)). Major advantages of SAR data to in situ measurements include the gain of spatial information over large areas, the opportunity to 'go back in time' by using archived data, and the lower cost of satellite images compared to the cost of installing an offshore meteorological mast. Disadvantages include the much lower frequency of satellite sampling and the fixed time of the day for satellite overpasses. Statistical analyses have shown that a total of 60-70 randomly selected samples are required for a robust estimate of the mean wind speed and the Weibull A parameter, whereas ~2000 samples are needed for assessment of Weibull k and the mean power density (Barthelmie & Pryor, 2003; Pryor et al., 2004). SAR samples are not randomly sampled. However, a general trend towards a larger availability and a decreasing cost per scene means that robust wind resource assessment from SAR images is becoming realistic. The issue is further discussed in Paper III.

Risø WEMSAR Tool
The Risø WEMSAR Tool (RWT) has been developed within the project EO-WINDFARM (2003-2006) for SAR wind resource assessment based on the WAsP concept of Weibull fitting (Nielsen et al., 2004). RWT requires an input of SAR-retrieved wind fields. As seen from Figure 10-1 (upper left panel), users have the opportunity to

view and select SAR wind maps, once they are loaded into RWT, and various settings can be changed.
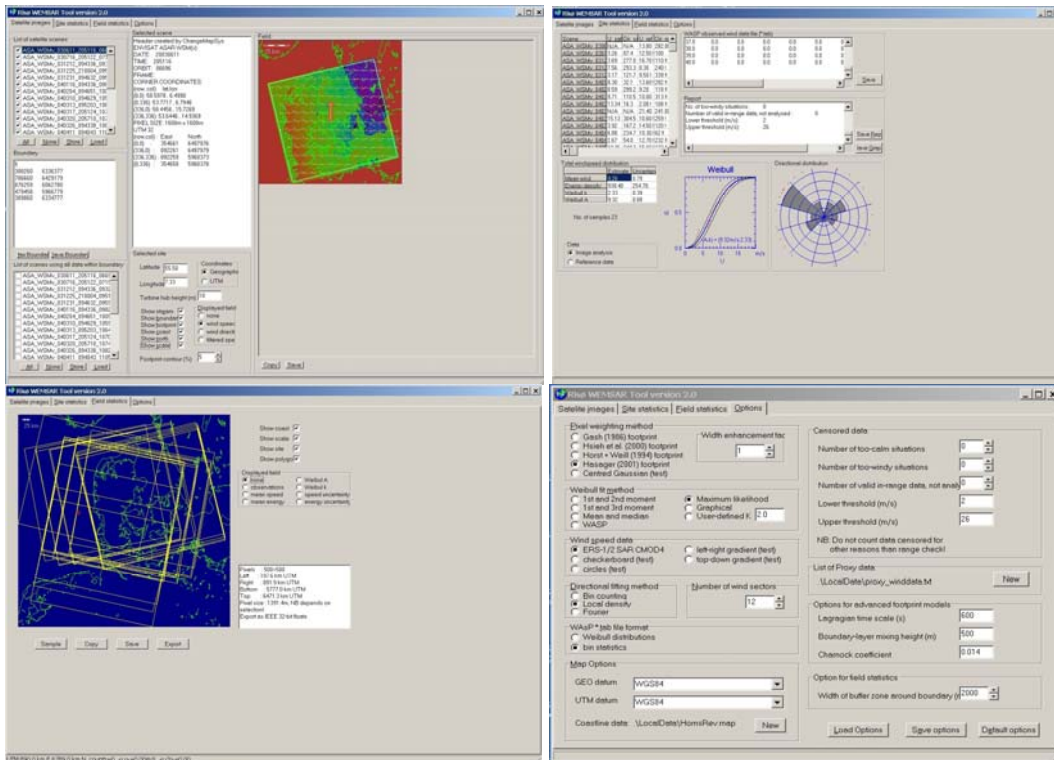

Figure 10-1. Risø WEMSAR Tool (RWT). Upper left: loading of SAR images; upper right: image statistics based on Weibull fitting; lower left: field statistics; lower right: options to be set by the user.

RWT uses footprint averaging to determine the 10 m wind speed at a given location (see Paper III or Hasager et al. (2004) for details). Based on the SAR wind fields, RWT outputs the wind distribution and Weibull parameters in various formats (Figure 10-1, upper right panel). One is a wind speed and directional distribution table, which may be opened in WAsP for further assessment studies analogous to studies based on in situ measurements. For example, one can create a wind farm and estimate its power output for different turbine types and layouts. Keeping the similarity principle in mind, it may be advantageous to base a WAsP analysis offshore on SAR measurements obtained at offshore locations rather than on a land mast.

Comparison of wind resources from SAR and in situ measurements
An optional feature in RWT allows users to load a list of in situ measurements of wind speed and direction, corresponding in time to loaded SAR data. The feature was utilized in this project to compare the wind resource predicted from SAR and in situ data, respectively for the Horns Rev site (Paper III). Wind fields were retrieved from the SAR images using in situ wind directions plus directions found with the LG method (see Section 6.4). Comparisons were made with the scalar footprint of RWT (Gash, 1986), as well as simple box averaging with and without a mask. The result was nine different estimates of the wind resource from the SAR data set of 91 scenes.

Mean wind speeds for the SAR data set agreed with the mean wind speed from in situ measurements to within ±15% for all wind retrieval methods. The accuracy on SAR mean wind speeds was closely linked to the bias on wind retrievals and the best approximation to the in situ measurements was thus found from the bias-free CMOD5 retrievals (see Section 6.4). The mean wind speed found from 91 samples corresponded very well to in situ measurements from longer time series published by Troen & Petersen (1989) and Sommer (2003). The power density predicted from SAR wind fields retrieved with CMOD-IFR2 agreed exactly with the corresponding prediction from in situ measurements (91 samples). The accuracy of the power density was found to depend largely on the standard deviation of wind speed retrievals.

As seen in Paper III (Figure 8), the fitting of a Weibull function becomes a major source of error when the number of samples is small. Errors associated with the fitting were typically estimated to ±0.4 m s^{-1} for the mean wind speed in addition to the error on wind retrievals. Despite the low number of samples compared to the recommended, a good agreement was found between the power predicted from SAR scenes and from longer time series of in situ data (Troen & Petersen, 1989). The issue of too few samples may be partly resolved as the C-band SAR data archives grow and images become available at a generally decreasing cost.

10.3 Key results on wind resource assessment

The following conclusions were drawn, based on the wind resource assessment study performed on SAR measurements:

- Robust estimates of the mean wind speed can be made from a series of ~100 randomly selected SAR scenes.
- The accuracy on mean wind speeds predicted from SAR data relies on the bias of SAR wind retrievals.
- The accuracy on power density estimates from SAR depends on the standard deviation of wind retrievals.
- The potential of SAR-based wind resource assessment is increasing, as more satellite data become available at a decreasing cost.

11 Introduction to papers

Paper I

Christiansen, M.B., & Hasager, C.B. (2005). Wake effects of large offshore wind farms identified from satellite SAR. *Remote Sensing of Environment, 98*, 251-268.

The aim of this paper was to quantify the spatial extent and magnitude of wind wakes downstream of the two large scale wind farms at Horns Rev and Nysted. Maps of wind speed were retrieved from ERS-2 SAR and Envisat ASAR scenes using the geophysical model function CMOD4. The SAR wind fields were analyzed for variations of the mean wind speed along wind-aligned transects crossing the two wind farms. Velocity deficits were 8-9% on average immediately downstream of the wind farms. The spatial extent of wind wakes was more the 20 km in some situations, depending on the ambient wind speed, the atmospheric stability, and the number of turbines in operation. The analysis revealed that some SAR scenes are unsuitable for wake analysis owing to current-bathymetry impacts on the Bragg wave amplitude, which determines the radar backscatter. Offshore wind farm sites are very exposed to this problem as they are generally build at shallow water depths.

Paper II

Christiansen, M.B., & Hasager, C.B. (2006). Using airborne and satellite SAR for wake mapping offshore. *Wind Energy, 9*, 437-455.

This paper describes an aircraft SAR campaign that was carried out over the wind farm at Horns Rev on 12 October 2003. As for Paper I, the aim was to quantify the wind farm wake effect. Data acquisition from an aircraft allowed measurements to be obtained at a time when wind conditions were ideal for the study and most of the wind turbines were running. The campaign coincided in time with an overpass of the ERS-2 satellite, therefore a comparison of measurements from satellite and airborne SAR was possible. Wind speeds were retrieved from both data types using the model function CMOD4. For aircraft data acquired with horizontal polarization, a hybrid model function was used to account for the lower backscattering compared to vertically polarized data. The aircraft measurements showed velocity deficits on the order of 20%, whereas estimated deficits were around 10% from the satellite data. One reason for the difference was that measured wind speeds were normalized with an upstream reference measurement (the meteorological mast) and with measurements along parallel transects in the SAR images, respectively.

Paper III

Christiansen, M.B., Koch, W., Horstmann, J., Hasager, C.B., & Nielsen, M. (2006). Wind resource assessment from C-band SAR. *Remote Sensing of Environment, 105*, 68-71.

Wind resource assessment studies based on SAR scenes are very sensitive to the absolute wind speed obtained from the SAR measurements. A study was carried out to determine the best choice of geophysical model function for accurate SAR wind retrievals. Three model functions were tested: CMOD-IFR2, CMOD4, and CMOD5. The wind direction input, necessary for the SAR wind retrievals, was obtained from three different sources: in situ measurements, a semi-automatic and an automatic analysis of image gradients caused by wind-aligned streaks. A total of 91 SAR images from ERS-2 and Envisat were

analyzed. The most accurate wind retrievals were performed with CMOD-IFR2 using in situ measurements of the wind direction. Winds were retrieved from this method with a standard deviation of 1.1 m s^{-1} and a bias of 0.3 m s^{-1}. The bias was associated with offshore winds and non-neutral atmospheric conditions mainly. The wind resource assessment based on the SAR data corresponded very well to the corresponding assessment from in situ data and to results from longer time series of measurements found in the literature. The work presented in this paper was carried out in collaboration with GKSS Research Center in Germany.

Paper IV
Hasager, C.B., Barthelmie, R.J., <u>Christiansen, M.B.</u>, Nielsen, M., & Pryor, S.C. (2006). Quantifying offshore wind resources from satellite wind maps: study area the North Sea. *Wind Energy, 9*, 63-74.

The purpose of this paper was to provide state-of-the-art information on satellite remote sensing applied to offshore wind energy. SAR-retrieved wind speeds obtained in the wake of the wind farm at Horns Rev were compared with wind speed predictions from an 'added roughness' wake model. Reasonable agreement was found from the preliminary comparison. In addition to wake and wind resource assessment studies from SAR data, the paper presents regional scale scatterometer measurements of wind speed and direction. The suitability of the two different data types (i.e. high-resolution SAR and coarser resolution scatterometry) with respect to wind energy applications is discussed.

Paper V
Monaldo, F.M., Thompson, D.R., Winstead, N.S., Pichel, W.G., Clemente-Colón, P, & <u>Christiansen, M.B.</u> (2006). Ocean wind field mapping from synthetic aperture radar and its application to research and applied problems. *Johns Hopkins APL Technical Digest*, *26*, 102-113.

This paper embraces several applications of high-resolution SAR data that are all relevant for wind energy purposes. A case study showing the wind farm wake effect at Horns Rev is presented with figures of the absolute wind speed variation along two transects. One transect crosses the wind farm at Horns Rev and the other is non-obstructed. A significant drop of the wind speed is seen for the first transect, whereas the second shows a more constant wind speed. Other applications of SAR data presented in the paper include the study of mesoscale phenomena such as gap flows and barrier jets. Knowledge about the phenomena is useful for a broad range of meteorological applications, including wind energy. This paper results from collaboration with the Johns Hopkins University, Applied Physics Laboratory in Maryland, USA.

Paper VI
<u>Christiansen, M.B.</u> (2004). Wind energy studies offshore using satellite remote sensing. 19th World Energy Congress 2004, Sydney (AU), 5-9 Sep 2004. Unpublished. 10 p.

The paper places the Ph.D. study in a broader context with figures on the global wind power status. The paper was written at an early stage of the Ph.D. project and describes very well the motivation behind the Ph.D. work: several challenges must be faced in the energy sector with respect to securing a sustainable energy supply for future generations. The paper was presented at the 19th World Energy Congress 2004 in Sydney, Australia.

Paper VII

Christiansen, M.B. & Hasager, C.B. (2005). Wake studies around a large offshore wind farm using satellite and airborne SAR. In: Proceedings (CD-ROM). 31st International Symposium on Remote Sensing of Environment: Global Monitoring for Sustainability and Security, St. Petersburg (RU), 20-24 Jun 2005. (Nansen International Environmental and Remote Sensing Centre, St. Petersburg, 2005) 4 p.

The topic of this paper is the airborne SAR campaign conducted at Horns Rev on 12 October 2003. The paper presents figures on the absolute wind speed variation along the five aircraft flight tracks acquired in C-band with vertical polarization. The paper was presented at the 31st International Symposium on Remote Sensing of Environment (2005) in St. Petersburg, Russia.

Paper VIII

Christiansen, M.B. & Hasager, C.B. (2006). Wind energy applications of synthetic aperture radar. In: Combined preprints (CD-ROM). 86th AMS Annual Meeting, Atlanta, GA (US), 29 Jan - 2 Feb 2006. (American Meteorological Society, Boston, MA, 2006) 6 p.

The paper was written at the final stage of the Ph.D. project and summarizes the work carried out to *i)* describe wind farm wake effects and *ii)* produce robust estimates of the wind resource from SAR measurements. An interesting result is presented in the form of a mean wind speed map covering the Danish inner seas from 20 Envisat ASAR scenes acquired in wide swath mode (400 km x 400 km coverage). The paper was presented at the 86th AMS Annual Meeting (2006) in Atlanta, US.

12 Conclusions and future perspectives

Results presented in this Ph.D. dissertation show that SAR measurements are, indeed, useful for several applications related to offshore wind energy. Observations over large areas, as provided by satellite images, cannot be gathered from any other data source. SAR images are thus complementary to in situ measurements that are costly and model data that are not fully verified. A lot can be learned about ocean wind fields simply by studying the variability in SAR wind maps. A good example is the wind field in Figure 9-3, which gives an immediate impression of the spatial extent and magnitude of wind farm wake effects. The image reveals that wind wakes may persist longer than predicted by state-of the-art wake models.

The next step is to quantify variations in the ocean wind field. This can, to a large extent, be done in relative terms without any major concerns about the absolute accuracy of SAR wind retrievals. For example, relative measurements are useful for comparing wake and non-wake areas. This was utilized in the Ph.D. project through computation of velocity deficits; and by others for comparisons of potential wind farm sites (Choisnard et al., 2004; Hasager et al., 2005; Schneiderhan et al., 2005). The absolute accuracy on satellite SAR wind retrievals was shown in this project to be sufficient for wind resource assessment in the early stage of wind farm planning. A remaining challenge is the projection of 10 m wind fields obtained from SAR measurements to wind turbine hub heights that are continuously increasing.

The opportunity of comparing SAR wind fields with wake model results was briefly addressed in this project. As the modeling of wake effects from large offshore wind farms and, particularly, the area downwind of the turbines matures, it would be interesting to make further comparisons with state-of-the-art models including the 'added roughness' approach as well as single wake models.

The field of mesoscale modeling is developing rapidly and the demand for data to verify the model results is growing. Preliminary comparisons of SAR and model data have been carried out (Badger et al., 2006; Beaucage et al., 2006). As the results were very promising and a large degree of similarity was found between the two types of data, further comparisons are planned. A project named NET-SAR has been proposed with the objective of comparing SAR and model wind fields for the entire Baltic Sea. The project will also lead to a SAR-based offshore wind atlas for the region.

For the purposes of this project, SAR data acquired in C-band were more attractive than e.g. L-band data because the relation between NRCS and wind speed is well described and validated. However, the L-band SAR data acquired from an aircraft over Horns Rev during the campaign on 12 October 2003 may be useful for other purposes and should be investigated further. Describing the strengths and limitations of L-band SAR data have become very relevant with the recent launch of the sensor PALSAR on board the Japanese ALOS satellite. Possible applications of the airborne SAR data set from Horns Rev may be the testing and further development of a model function that relates L-band SAR signals to wind speed (Shimada et al., 2003; Shimada et al., 2004). Alternatively, the data could be used to separate atmospheric (e.g. wind speed) and oceanic (e.g. current-bathymetry) influences on SAR measurements.

References

Alpers, W., Campbell, G., Wensink, H., & Zhang, Q. (2004). Underwater Topography. In C.R.Jackson, & J.R.Apel (Eds.), *Synthetic Aperture Radar Marine User's Manual* (pp. 245-262). Washington, DC: U.S. Department of Commerce, National Oceanic and Atmospheric Administration.

Alpers, W., & Espedal, H. A. (2004). Oils and surfactants. In C.R.Jackson, & J.R.Apel (Eds.), *Synthetic Aperture Radar Marine User's Manual* (pp. 263-275). Washington, DC: U.S. Department of Commerce, National Oceanic and Atmospheric Administration.

Alpers, W., & Hennings, I. (1984). A theory of the imaging mechanism of underwater bottom topography by real and synthetic aperture radar. *Journal of Geophysical Research*, *89*, 529-546.

Alpers, W., & Melsheimer, C. (2004). Rainfall. In C.R.Jackson, & J.R.Apel (Eds.), *Synthetic Aperture Radar Marine User's Manual* (pp. 355-371). Washington, DC: U.S. Department of Commerce, National Oceanic and Atmospheric Administration.

Alpers, W. R., Ross, D. B., & Rufenach, C. L. (1981). On the detectability of ocean surface-waves by real and synthetic aperture radar. *Journal of Geophysical Research-Oceans and Atmospheres*, *86*, 6481-6498.

Apel, J. R. (2004). Oceanic internal waves and solitions. In C.R.Jackson, & J.R.Apel (Eds.), *Synthetic Aperture Radar Marine User's Manual* (pp. 189-206). Washington, DC: U.S. Department of Commerce, National Oceanic and Atmospheric Administration.

Atlas, D. (1994). Footprints of storms on the sea - a view from spaceborne synthetic-aperture radar. *Journal of Geophysical Research-Oceans*, *99*, 7961-7969.

Badger, J., Barthelmie, R., Frandsen, S., & Christiansen, M. B. (2006). Mesoscale modelling for an offshore wind farm. *Proceedings, 2006 European Wind Energy Conference and Exhibition, Athens (GR), 27 February - 2 March 2006*, CD-ROM.

Barthelmie, R., Larsen, G., Pryor, S., Jørgensen, H., Bergstrom, H., Magnusson, M., Schlez, W., Rados, K., Lange, B., Vølund, P., Neckelmann, S., Mogensen, S., Schepers, G., Hegberg, T., & Folkerts, L. (2003a). *Efficient Development of Offshore Wind Farms (ENDOW)* (pp. 1-29). Roskilde: Risø National Laboratory. Risø-R-1407(EN).

Barthelmie, R., Larsen, G., Pryor, S., Jorgensen, H., Bergstrom, H., Schlez, W., Rados, K., Lange, B., Volund, P., Neckelmann, S., Mogensen, S., Schepers, G., Hegberg, T., Folkerts, L., & Magnusson, M. (2004a). ENDOW (Efficient development of offshore wind farms): Modelling wake and boundary layer interactions. *Wind Energy*, *7*, 225-245.

Barthelmie, R. J., Courtney, M. S., Højstrup, J., & Larsen, S. E (1996). Meteorological aspects of offshore wind energy: observations from the

Vindeby wind farm. *Journal of Wind Engineering and Industrial Aerodynamics*, *62*, 191-211.

Barthelmie, R. J., Courtney, M. S., Højstrup, J., & Sanderhoff, P. (1994). *The Vindeby project: a description.* Roskilde: Risø National Laboratory. Risø-R-741(EN).

Barthelmie, R. J., Folkerts, L., Ormel, F. T., Sanderhoff, P., Eecen, P. J., Stobbe, O., & Nielsen, N. M. (2003b). Offshore wind turbine wakes measured by sodar. *Journal of Atmospheric and Oceanic Technology*, *20*, 466-477.

Barthelmie, R. J., Frandsen, S. T., Rethore, P.-E., Mechali, M., Pryor, S. C., Jensen, L., & Sørensen, P. (2006). Modeling and measurements of offshore wakes. *Proceedings, OWEMES, Citavecchia (I), 20-22 April 2006*.

Barthelmie, R. J., & Giebel, G. (2006). Prediction of wind speed profiles for short-term forecasting in the offshore environment. *Proceedings, 2006 European Wind Energy Conference and Exhibition, Athens (GR), 27 February - 2 March 2006*, CD-ROM.

Barthelmie, R. J., & Pryor, S. C. (2003). Can satellite sampling of offshore wind speeds realistically represent wind speed distributions. *Journal of Applied Meteorology*, *42*, 83-94.

Barthelmie, R. J., & Pryor, S. C. (2006). Challenges in predicting power output from offshore wind farms. *Journal of Energy Engineering on Sustainable Energy Systems*, *in press*.

Barthelmie, R. J., Pryor, S. C., Frandsen, S., & Larsen, S. (2004b). Analytical and empirical modelling of flow downwind of large wind farm clusters. *Proceedings, Special Topic Conference: The science of making torque from wind, Delft (NL)*, 292-303.

Beaucage, P., Glazer, A., Yu, W., Benoit, R., Lafrance, G., & Bernier, M. (2006). Wind assessment using synthetic aperture radar (SAR) satellite and the mesoscale compressible community (MC2) model. *Proceedings, 2006 European Wind Energy Conference and Exhibition, Athens, Greece, 27 February - 2 March 2006*, CD-ROM.

Brown, R. A. (2000a). On satellite scatterometer model functions. *Journal of Geophysical Research*, *105*, 29195-29205.

Brown, R. A. (2000b). Serendipity in the use of satellite scatterometer, SAR and other sensor data. *Johns Hopkins Apl Technical Digest*, *21*, 21-26.

Brown, R. A. (2002). Scaling effects in remote sensing applications and the case of organized large eddies. *Canadian Journal of Remote Sensing*, *28*, 340-345.

Charnock, H. (1955). Wind stress on a water surface. *Quarterly Journal of the Royal Meteorological Society*, *81*, 639-640.

Choisnard, J., Lafrance, G., & Bernier, M. (2004). SAR-satellite for offshore and coastal wind resource analysis, with examples from St. Lawrence Gulf, Canada. *Wind Engineering*, *28*, 367-382.

Chunchuzov, I., Vachon, P. W, & Li, X. (2000). Analysis and modeling of atmospheric gravity waves observed in RADARSAT SAR images. *Remote Sensing of Environment*, *74*, 343-361.

Crespo, A., Hernandez, J., & Frandsen, S. (1999). Survey of modelling methods for wind turbine wakes and wind farms. *Wind Energy*, *2*, 1-24.

Danish Energy Authority (2005). *Offshore Wind Power - Danish Experiences and Solutions* (pp. 1-32). Copenhagen.

Du, Y., Vachon, P. W., & Wolfe, J. (2002). Wind direction estimation from SAR images of the ocean using wavelet analysis. *Canadian Journal of Remote Sensing*, *28*, 498-509.

Elfouhaily, T. M. (1996). *Modéle couple vent/vagues et son application à la télédétection par micro-onde de la surface de la mer*. Paris: University of Paris VII. Ph.d. thesis (in English).

Espedal, H. A., Johannessen, O. M., Johannessen, J., Dano, E., Lyzenga, D. R., & Knulst, J. C. (1998). COASTWATCH'95: ERS 1/2 SAR detection of natural film on the ocean surface. *Journal of Geophysical Research-Oceans*, *103*, 24969-24982.

Espedal, H. A., Johannessen, O. M., & Knulst, J. (1996). Satellite detection of natural films on the ocean surface. *Geophysical Research Letters*, *23*, 3151-3154.

Fichaux, N., & Ranchin, T. (2002). Combined extraction of high spatial resolution wind speed and direction from SAR images: a new approach using wavelet transform. *Canadian Journal of Remote Sensing*, *28*, 510-516.

Folkerts, L., Barthelmie, R. J., Sanderhoff, P., Ormel, F. T., Eecen, P. J., & Stobbe, O. (2001). Sodar measurements of offshore wakes. *Wind Engineering*, *25*, 301-306.

Frandsen, S., Barthelmie, R., Pryor, S., Rathmann, O., Larsen, S., Højstrup, J., & Thøgersen, M. (2006). Analytical modelling of wind speed deficit in large offshore wind farms. *Wind Energy*, *9*, 39-53.

Frandsen, S., Chacon, L., Crespo, A., Enevoldsen, P., Gomez-Elvira, R., Hernandez, J., Højstrup, J., Manuel, F., Thomsen, K., & Sørensen, P. (1996). *Measurements on and modelling of offshore wind farms*. Roskilde, Denmark: Risø National Laboratory. Risø-R-903(EN).

Frandsen, S., & Christensen, J. C. (1994). Vindeby offshore wind farm - fatique measurements. *Proceedings, 1994 European Wind Energy Conference, Thessaloniki (GR), 10-14 October 1994*, 397-401.

Frandsen, S., & Thomsen, K. (1997). Change in fatique and extreme loading when moving wind farms offshore. *Wind Engineering*, *21*, 197-214.

Frandsen, S. T. (2006). *Turbulence and turbulence-generated structural loading in wind turbine clusters* (pp. 1-126). Roskilde: Risø National Laboratory. Risø-R-1188(EN).

Fu, L. L., & Holt, B. (1982). *Seasat views oceans and sea ice with synthtic-aperture radar* (pp. 1-200). Pasadena, CA: Jet Propulsion Laboratory Publication 81-120.

Furevik, B., Johannessen, O., & Sandvik, A. D. (2002). SAR-retrieved wind in polar regions - comparison with in situ data and atmospheric model output. *IEEE Transactions on Geoscience and Remote Sensing*, *40*, 1720-1732.

Furevik, B. R., Hasager, C. B., Nielsen, M., Hamre, T., Jørgensen, B. H., Rathmann, O., & Johannessen, O. M. (2003). Radar remote sensing in offshore wind resource assessment. *Proceedings of the Second Workshop on Coastal and Marine Applications of SAR, 8-12 September 2003, Svalbard (N)*, CD-ROM.

Gade, M., Alpers, W., Ermakov, S. A., Hühnerfuss, H., & Lange, P. A. (1998a). Wind-wave tank measurements of bound and freely propagating short gravity capillary waves. *Journal of Geophysical Research-Oceans*, *103*, 21697-21709.

Gade, M., Alpers, W., Hühnerfuss, H., & Lange, P. A. (1998b). Wind wave tank measurements of wave damping and radar cross sections in the presence of monomolecular surface films. *Journal of Geophysical Research-Oceans*, *103*, 3167-3178.

Gade, M., Alpers, W., Hühnerfuss, H., Masuko, H., & Kobayashi, T. (1998c). Imaging of biogenic and anthropogenic ocean surface films by the multifrequency/multipolarization SIR-C/X-SAR. *Journal of Geophysical Research-Oceans*, *103*, 18851-18866.

Gade, M., Alpers, W., Hühnerfuss, H., Wismann, V. R., & Lange, P. A. (1998d). On the reduction of the radar backscatter by oceanic surface films: scatterometer measurements and their theoretical interpretation. *Remote Sensing of Environment*, *66*, 52-70.

Garrat, J. R. (1990). The internal boundary layer - a review. *Boundary-Layer Meteorology*, *50*, 171-203.

Garratt, J. R. (1992). *The Atmopsheric Boundary Layer* (pp. 1-316). New York: Cambridge University Press.

Gash, J. H. C. (1986). A note on estimating the effect of a limited fetch on micrometeorological evaporation measurements. *Boundary-Layer Meteorology*, *35*, 409-413.

Gerling, T. W. (1986). Structure of the surface wind field from the SEASAT SAR. *Journal of Geophysical Research*, *91*, 2308-2320.

Giebel, G., Brownsword, R., & Kariniotakis, G. (2003). *The state-of-the-art in short-term prediction of wind power. A literature overview*. http://anemos.cma.fr/download/ANEMOS_D1.1_StateOfTheArt_v1.1.pdf.

Gryning, S. E., Batchvarova, E., & Landberg, L. (2006). Wind profile over homogeneous terrain beyond the surface boundary layer. *Proceedings, 2006 European Wind Energy Conference and Exhibition, Athens (GR), 27 February - 2 March 2006*, CD-ROM.

Hasager, C. B., Astrup, P., Christiansen, M. B., Nielsen, M., & Barthelmie, R. (2006). Wind resources and wind farm wake effects offshore observed from

satellite. *Proceedings, 2006 European Wind Energy Conference and Exhibition, Athens (GR), 27 February - 2 March 2006*, CD-ROM.

Hasager, C. B., Dellwik, E., Nielsen, M., & Furevik, B. (2004). Validation of ERS-2 SAR offshore wind-speed maps in the North Sea. *International Journal of Remote Sensing*, *25*, 3817-3841.

Hasager, C. B., Frank, H. P., & Furevik, B. R. (2002). On offshore wind energy mapping using satellite SAR. *Canadian Journal of Remote Sensing*, *28*, 80-89.

Hasager, C. B., Nielsen, M., Astrup, P., Barthelmie, R. J., Dellwik, E., Jensen, N. O., Jørgensen, B. H., Pryor, S. C., Rathmann, O., & Furevik, B. (2005). Offshore wind resource estimation from satellite SAR wind field maps. *Wind Energy*, *8*, 403-419.

Hasselmann, K., Raney, R. K., Plant, W. J., Alpers, W., Shuchman, R. A., Lyzenga, D. R., Rufenach, C. L., & Tucker, M. J. (1985). Theory of synthetic aperture radar ocean imaging - a marsen view. *Journal of Geophysical Research-Oceans*, *90*, 4659-4686.

He, Y. J., Perrie, W., Zou, Q. P., & Vachon, P. W. (2005). A new wind vector algorithm for C-band SAR. *IEEE Transactions on Geoscience and Remote Sensing*, *43*, 1453-1458.

Hersbach, H. (2003). *CMOD5. An improved geophysical model function for ERS C-band scatterometry* (pp. 1-50). Reading, UK: ECMWF Technical Memorandum 395.

Højstrup, J. (1999). Spectral coherence in wind turbine wakes. *Journal of Wind Engineering and Industrial Aerodynamics*, *80*, 137-146.

Holt, B. (2004). SAR imaging of the ocean surface. In C.R.Jackson, & J.R.Apel (Eds.), *Synthetic Aperture Radar Marine User's Manual* (pp. 25-79). Washington, DC: U.S. Department of Commerce, National Oceanic and Atmospheric Administration.

Horstmann, J., Koch, W., Lehner, S., & Tonboe, R. (2000a). Wind retrieval over the ocean using synthetic aperture radar with C-band HH polarization. *IEEE Transactions on Geoscience and Remote Sensing*, *38*, 2122-2131.

Horstmann, J., Koch, W., Lehner, S., & Tonboe, R. (2002). Ocean winds from RADARSAT-1 ScanSAR. *Canadian Journal of Remote Sensing*, *28*, 524-533.

Horstmann, J., Lehner, S., Koch, W., & Tonboe, R. (2000b). Computation of wind vectors over the ocean using spaceborne syntheric aperture radar. *Johns Hopkins Apl Technical Digest*, *21*, 100-107.

Horstmann, J., Schiller, H., Schulz-Stellenfleth, J., & Lehner, S. (2003). Global wind speed retrieval from SAR. *IEEE Transactions on Geoscience and Remote Sensing*, *41*, 2277-2286.

Horstmann, J., Thompson, D. R., Monaldo, F., Iris, S., & Graber, H. C. (2005). Can synthetic aperture radars be used to estimate hurricane force winds? *Geophysical Research Letters*, *32*.

IEA (2005). *IEA Wind Energy Annual Report 2004* (pp. 1-264). http://www.ieawind.org.

Johannessen, J., Shuchman, R. A., Digranes, G., Lyzenga, D. R., Wackerman, C., Johannessen, O. M., & Vachon, P. W. (1996). Coastal ocean fronts and eddies imaged with ERS 1 synthetic aperture radar. *Journal of Geophysical Research-Oceans*, *101*, 6651-6667.

Koch, F. W., Erlich, I., Shewarega F., & Bachmann U. (2003a). Dynamic Interaction of Large Offshore Wind Farms With the Electric Power System. *Bologna PowerTech (Bologna, Italy)*.

Koch, F. W., Erlich, I., Shewarega F., & Bachmann U. (2003b). Simulation of the Dynamic Interaction of Large Offshore Wind Farms With the Electric Power System. *OWEMES 2003, Naples (I)*.

Koch, W. (2004). Directional analysis of SAR images aiming at wind direction. *IEEE Transactions on Geoscience and Remote Sensing*, *42*, 702-710.

Lange, B., Larsen, S., Højstrup, J., & Barthelmie, R. (2004a). Importance of thermal effects and sea surface roughness for offshore wind resource assessment. *Journal of Wind Engineering and Industrial Aerodynamics*, *92*, 959-988.

Lange, B., Larsen, S., Højstrup, J., & Barthelmie, R. (2004b). The influence of thermal effects on the wind speed profile of the coastal marine boundary layer. *Boundary-Layer Meteorology*, *112*, 587-617.

Lehner, S., Horstmann, J., Koch, W., & Rosenthal, W. (1998). Mesoscale wind measurements using recalibrated ERS SAR images. *Journal of Geophysical Research - Oceans*, *103*, 7847-7856.

Lewis, A. J., & Henderson, F. M. (1998). Radar fundamentals: the geoscience perspective. In F. M. Henderson, & A. J. Lewis (Eds.), *Principles and Applications of Imaging Radar. Manual of remote sensing, 3rd Edition, Vol. 2* (pp. 131-176). New York: Wiley.

Li, X. (2004). Atmospheric vortex streets and gravity waves. In C.R.Jackson, & J.R.Apel (Eds.), *Synthetic Aperture Radar Marine User's Manual* (pp. 341-352). Washington, DC: U.S. Department of Commerce, National Oceanic and Atmospheric Administration.

Li, X., Clemente-Colon, P., Pichel, W., & Vachon, P. W (2000). Atmospheric vortex streets on a RADARSAT SAR image. *Geophysical Research Letters*, *27*, 1655-1658.

Lyzenga, D. R. (1991). Interaction of Short Surface and Electromagnetic-Waves with Ocean Fronts. *Journal of Geophysical Research-Oceans*, *96*, 10765-10772.

Melsheimer, C., Alpers, W., & Gade, M. (1998). Investigation of multifrequency/multipolarization radar signatures of rain cells over the ocean using SIR-C/X-SAR data. *Journal of Geophysical Research-Oceans*, *103*, 18867-18884.

Monaldo, F. (2000). The Alaska SAR demonstration and near-real-time synthetic aperture radar winds. *Johns Hopkins Apl Technical Digest*, *21*, 75-79.

Monaldo, F., & Kerbaol, V. (2003). The SAR measurement of ocean winds: an overview for the 2nd workshop on coastal and marine applications of SAR. *Proceedings of the Second Workshop on Coastal and Marine Applications of SAR, 8-12 September 2003, Svalbard (N)*.

Monaldo, F. M., & Beal, R. (2004). Wind speed and direction. In C.R.Jackson, & J.R.Apel (Eds.), *Synthetic Aperture Radar Marine User's Manual* (pp. 305-320). Washingon, DC: U.S. Department of Commerce, National Oceanic and Atmospheric Administration.

Monaldo, F. M., Thompson, D. R., Beal, R. C., Pichel, W. G., & Clemente-Colón, P. (2001). Comparison of SAR-derived wind speed with model predictions and ocean buoy measurements. *IEEE Transactions on Geoscience and Remote Sensing*, *39*, 2587-2600.

Monaldo, F. M., Thompson, D. R., Pichel, W. G., & Clemente-Colon, P. (2004). A systematic comparison of QuikSCAT and SAR ocean surface wind speeds. *IEEE Transactions on Geoscience and Remote Sensing*, *42*, 283-291.

Mortensen, N. G., Hansen, J. C., Badger, J., Jørgensen, B. H., Hasager, C. B., Youssef, L. G., Said, U. S., Moussa, A. A. E., Mahmoud, M. A., Yousef, A. E. S., Awad, A. M., Ahmed, M. A. R., Sayed, M. A. M., Korany, M. H., & Tarad, M. A. B. (2006). *Wind Atlas for Egypt. Measurements and Modelling 1991-2005* (pp. 1-258). Roskilde: Risø National Laboratory.

Mortensen, N. G., Heathfield, D. N., Myllerup, L., Landberg, L., & Rathmann, O. (2005). *Wind Atlas Analysis and Application Program: WAsP 8 Help Facility*. Roskilde, Denmark: Risø National Laboratory.

Motta, M., Barthelmie, R. J., & Vølund, P. (2005). The influence of non-logarithmic wind speed profiles on potential power output at Danish offshore sites. *Wind Energy*, *8*, 219-236.

Mouche, A. A., Hauser, D., Daloze, J. F., & Guerin, C. (2005). Dual-polarization measurements at C-band over the ocean: Results from airborne radar observations and comparison with ENVISAT ASAR data. *IEEE Transactions on Geoscience and Remote Sensing*, *43*, 753-769.

Nielsen, M., Astrup, P., Hasager, C. B., Barthelmie, R. J., & Pryor, S. C. (2004). *Satellite information for wind energy applications* (pp. 1-57). Roskilde, Denmark: Risø National Laboratory. Risø-R-1479(EN).

Petersen, E. L., Mortensen, N. G, Landberg, L., Højstrup, J., & Frank, H. P. (1998). Wind power meteorology: Part I. Climate and turbulence. *Wind Energy*, *1*, 2-22.

Pryor, S. C., Nielsen, M., Barthelmie, R. J., & Mann, J. (2004). Can satellite sampling of offshore wind speeds realistically represent wind speed distributions? Part II: Quantifying uncertainties associated with sampling strategy and distribution fitting methods. *Journal of Applied Meteorology*, *43*, 739-750.

Quilfen, Y., Chapron, B., Elfouhaily, T., Katsaros, K., & Tournadre, J. (1998). Observation of tropical cyclones by high-resolution scatterometry. *Journal of Geophysical Research*, *103*, 7767-7786.

Raney, R. K. (1998). Radar fundamentals: technical perspective. In F. M. Henderson, & A. J. Lewis (Eds.), *Principles and Applications of Imaging Radar. Manual of remote sensing, 3rd Edition, Vol. 2* (pp. 9-130). New York: Wiley.

Rathmann, O., Barthelmie, R., & Frandsen, S. (2006). Turbine wake model for wind resource software. *European Wind Energy Conference and Exhibition, Athens (GR), 27 February - 2 March 2006*.

Romeiser, R., & Alpers, W. (1997). An improved composite surface model for the radar backscattering cross section of the ocean surface. 2: Model response to surface roughness variations and the radar imaging of underwater bottom topography. *Journal of Geophysical Research-Oceans*, *102*, 25251-25267.

Schmidt, A., Wismann, V., Romeiser, R., & Alpers, W. (1995). Simultaneous measurements of the ocean wave-radar modulation transfer function at L, C, and X bands from the research platform Nordsee. *Journal of Geophysical Research*, *100*, 8815-8827.

Schneiderhan, T., Lehner, S., Schulz-Stellenfleth, J., & Horstmann, J. (2005). Comparison of offshore wind park sites using SAR wind measurement techniques. *Meteorological Applications*, *12*, 101-110.

Shimada, T., Kawamura, H., & Shimada, M. (2003). An L-band geophysical model function for SAR wind retrieval using JERS-1 SAR. *IEEE Transactions on Geoscience and Remote Sensing*, *41*, 518-531.

Shimada, T., Kawamura, H., Shimada, M., Watabe, I., & Iwasaki, S. I. (2004). Evaluation of JERS-1 SAR images from a coastal wind retrieval point of view. *IEEE Transactions on Geoscience and Remote Sensing*, *42*, 491-500.

Sikora, T. D., & Thompson, D. R. (2002). Air-sea turbulence statistics from synthetic aperture radar: An update. *Canadian Journal of Remote Sensing*, *28*, 517-523.

Sikora, T. D., & Ufermann, S. (2004). Marine atmospheric boundary layer cellular convection and longitudinal roll vortices. In C.R.Jackson, & J.R.Apel (Eds.), *Synthetic Aperture Radar Marine User's Manual* (pp. 321-330). Washington, DC: U.S. Department of Commerce, National Oceanic and Atmospheric Administration.

Sommer, A. (2003). Offshore measurements of wind and waves at Horns Rev and Laesoe, Denmark. *OWEMES, 10-12 April 2003, Naples (I)*, 65-79.

Stoffelen, A., & Anderson, D. L. T. (1997). Scatterometer data interpretation: Estimation and validation of the transfer fuction CMOD4. *Journal of Geophysical Research*, *102*, 5767-5780.

Stull, R. B. (1991). *An Introduction to Boundary Layer Meteorology* (pp. 1-666). Dordrecht: Kluwer Academic Puhlishers.

Thompson, D., Elfouhaily, T., & Chapron, B. (1998). Polarization ratio for microwave backscattering from the ocean surface at low to moderate incidence angles. *Proceedings International Geoscience and Remote Sensing Symposium, Seattle, WA*, 1671-1676.

Thompson, D. R., Monaldo, F. M., Elfouhaily, T. M., Farrar, J. T., Weller, R. A., & Grimmett, T. K. (2004). Comparison of high-resolution wind maps from SAR imagery with in-situ measurements from the ONR CBLAST experiments. *Proceedings International Geoscience and Remote Sensing Symposium, Anchorage, 20-24 September 2004*.

Troen, I., & Petersen, E. L. (1989). *European Wind Atlas* (pp. 1-656). Roskilde: Risø National Laboratory.

Troldborg, N., Sørensen, J. N., & Mikkelsen, R. (2006). Numerical simulations of wakes of wind turbines in wind farms. *Proceedings, 2006 European Wind Energy Conference and Exhibition, Athens (GR), 27 February - 2 March 2006*, CD-rom.

Ufermann, S., & Romeiser, R. (1999). A new interpretation of multifrequency/multipolarization radar signatures of the Gulf Stream front. *Journal of Geophysical Research*, *104*, 25697-25705.

Ulaby, F. W., Moore, R. K., & Fung, A. K. (1982). *Microwave Remote Sensing, Active and Passive. Volume II: Radar Remote Sensing and Surface Scattering Emission Theory* (pp. 457-1064). Reading, Massachusetts: Addison-Wesley.

Vachon, P. W., & Dobson, F. W. (1996). Validation of wind vector retrieval from ERS-1 SAR images over the ocean. *Global Atmosphere and Ocean System*, *5*, 177-187.

Vachon, P. W., Monaldo, F. M., Holt, B., & Lehner, S. (2004). Ocean surface waves and spectra. In C.R.Jackson, & J.R.Apel (Eds.), *Synthetic Aperture Radar Marine User's Manual* (pp. 139-169). Washington, DC: U.S. Department of Commerce, National Oceanic and Atmospheric Administration.

Vachon, P. W., & Dobson, E. W. (2000). Wind retrieval from RADARSAT SAR images: selection of a suitable C-band HH polarization wind retrieval model. *Canadian Journal of Remote Sensing*, *26*, 306-313.

Valenzuela, G. R. (1978). Theories for the interaction of electromagnetic and ocean waves - A review. *Boundary-Layer Meteorology*, *13*, 61-85.

Young, G., & Winstead, N. (2005). Meteorological phenomena in high resolution SAR wind imagery. In B.Beal, G.Young, F.Monaldo, D.Thompson, N.Winstead, & C.Scott (Eds.), *High Resolution Wind Monitoring with Wide Swath SAR: A User's Guide* (pp. 13-34). Washington, DC: U.S. Department of Commerce, National Oceanic and Atmospheric Administration.

Young, G. S. (2000). SAR signatures of the marine atmospheric boundary layer: implications for numerical forecasting. *John Hopkins APL Technical Digest*, *21*, 27-32.

Young, G. S., Kristovich, D. A. R., Hjelmfelt, M. R., & Foster, R. C. (2002). Rolls, streets, waves, and more: A review of quasi-two dimesional structures in the atmospheric boundary layer. *Bulletin of the American Meteorological Society*, *83*, 997-1001.

Young, G. S., Sikora, T. D., & Winstead, N. S. (2000). Inferring marine atmospheric boundary layer properties from spectral characteristics of satellite-borne SAR imagery. *Monthly Weather Review, 128*, 1520.

Risø's research is aimed at solving concrete
problems in the society.

Research targets are set through continuous
dialogue with business, the political system and
researchers.

The effects of our research are sustainable energy
supply and new technology for the health
sector.

www.risoe.dk